Single- and Multipoint Aerodynamic Shape Optimization Using Multifidelity Models and Manifold Mapping

Jethro Nagawkar *, Jie Ren †, Xiaosong Du ‡, and Leifur Leifsson § *Iowa State University, Ames, Iowa, United States, 50011*

Slawomir Koziel \P Reykjavik University, Menntavegur 1, 101 Reykjavik, Iceland

In this work, a computationally efficient multifidelity local search algorithm for aerodynamic design optimization is presented. In our approach, direct optimization of a computationally expensive model is replaced by an iterative updating and re-optimization of a fast multifidelity model constructed using a low-fidelity model adapted locally using manifold mapping (MM) to become a reliable representation of the high-fidelity one during the optimization process. Only one high-fidelity model evaluation is needed per design iteration and no gradient information is utilized. The proposed method is validated and characterized by applying it to a few single- and multipoint optimization problems involving inviscid and viscous transonic flows. The proposed method is compared with the sequential least squares programming (SLSQP) gradient-based approach with the gradients calculated based on adjoint sensitivities. In the inviscid single-point test case, a drag reduction of 410.8 counts was achieved by the MM algorithm while requiring approximately 1,469 min on a high performance computing (HPC) with 32 processors. SLSQP with adjoints achieved a drag reduction of 425.9 counts, while requiring approximately 1,536 min under the same HPC setup. For the viscous single-point test case, a 83.2 drag count reduction was reported for the MM compared to 83.4 for SLSQP with adjoints. In that case, the MM algorithm was around eight times faster in terms of computing time. In the multipoint design test case, the MM algorithm was computationally cheaper by at least an order of magnitude compared to SLSQP with adjoints, although the objective function value was around three drag counts higher. Furthermore, it was found that in the multipoint cases, the MM algorithm scales favorably with the number of operational conditions considered compared to SLSOP with adjoints.

^{*}PhD student, Department of Aerospace Engineering, AIAA student member.

[†]Masters student, Department of Aerospace Engineering, AIAA student member.

[‡]PhD student, Department of Aerospace Engineering, AIAA student member.

[§] Associate Professor, Department of Aerospace Engineering, AIAA senior member, corresponding author: leifur@iastate.edu.

[¶]Professor, Engineering Optimization & Modeling Center, AIAA senior member.

Nomenclature

A = Airfoil cross sectional area [-]

 $A_{baseline}$ = Baseline cross sectional area [-]

 A_{min} = Minimum cross sectional area [-]

 C_d = Drag coefficient [-]

 $C_{d.f}$ = Drag coefficient of high-fidelity model [-]

 C_l = Lift coefficient [-]

 $C_{l.f}$ = Lift coefficient of high-fidelity model [-]

 C_m = Pitching moment coefficient [-]

 $C_{m.f}$ = Pitching moment coefficient of high-fidelity model [-]

 C_p = Pressure coefficient [-]

c = low-fidelity model

D = Drag[N]

f = high-fidelity model

 $g(\mathbf{x})$ = Inequality constraints

 $h(\mathbf{x})$ = Equality constraints

H = Scalar valued objective function

l = Design variable lower bound

L = Lift[N]

M = Mach number [-]

 M_{∞} = Free stream Mach number [-]

P = Coordinates of the FFD control points

S = Response correction matrix

s = Surrogate model

u = Design variable upper bound

X = x location of B-spline control point

 \bar{X} = Airfoil coordinates from FFD control points

X = B-spline control polygon coordinates

x = Design variables

 $\mathbf{x}^{(0)}$ = Baseline design variables

x* = Optimized design variables

x = Airfoil chord-wise location [-]

Y = B-spline control polygon coordinates

y = Airfoil thickness [-]

 $\nabla f(\mathbf{x})$ = Gradient of objective function f

 δ = Trust region radius [-]

 ϵ_x = Argument termination criteria

 ϵ_H = Objective function termination criteria

 ϵ_{δ} = Trust region radius termination criteria

 $\Delta \mathbf{F}$ = Difference vector of high-fidelity model

 $\Delta \mathbf{C}$ = Difference vector of low-fidelity model

 $\Delta \mathbf{C}^{\dagger}$ = Pseudoinverse of $\Delta \mathbf{C}$

 $V_{\Delta C}$ = Decomposition factor of matrix ΔC

 $\sum_{\Delta \mathbf{C}}^{\dagger}$ = Decomposition factor of matrix $\Delta \mathbf{C}$

 $\mathbf{U}_{\Lambda \mathbf{C}}^{T}$ = Decomposition factor of matrix $\Delta \mathbf{C}$

 α = Angle of attack [degree]

 τ = Weight factor in multipoint design [-]

I. Introduction

A aircraft and wind turbines, see, e.g., [1] and [2]. Nowadays, the use of high-fidelity partial differential equation (PDE) simulations within the design process is becoming the standard. Typically, the main purpose of using high-fidelity PDE simulations is to capture any nonlinear physics encountered by the system. Moreover, it may be impossible to rely on prior designs when considering unconventional configurations. In addition, there may be nonlinear couplings with other disciplines. Therefore, high-fidelity PDE simulations are essential in modern engineering design.

It is challenging to use high-fidelity PDE simulations as a part of the design process. Design optimization using numerical techniques is not widely used in industry. In typical engineering practices, computational models are used in hands-on parametric studies. One of the reasons for optimization not being widespread is that the sheer computational cost can be so high that performing automated design optimization in a timely manner may not be possible, even when using high performance computing (HPC). The key challenges with automated PDE-constrained design optimization can be summarized as follows: (1) time-consuming PDE simulations, (2) large number of design variables, and (3) conventional optimization techniques require many model evaluations.

Direct design is a common approach to simulation-based aerodynamic design. Here, the designer manipulates the shape of the aerodynamic surface to directly minimize (or maximize) a given figure of merit subject to a set of constraints.

In wing (or airfoil) design, this is done for a given lift coefficient, Mach number, and Reynolds number. Essentially, this is a single-point, single-objective constrained nonlinear minimization problem. On the other hand, transport aircraft operate at various operating conditions due to different flight environment and fuel burn requirements [3]. Near the region where single-point design performs well, efficiency may increase dramatically with small changes in operating conditions [4]. So, instead of designing for a single point the design can be performed at all the required operating points. Leading to the so-called multipoint design [5], which essentially is a multipoint, single-objective constrained nonlinear minimization problem.

In aerodynamic design, the underlying problem can be formulated as a constrained nonlinear minimization problem. The task is to solve the minimization problem to yield the optimal aerodynamic design. This is known as aerodynamic shape optimization (ASO). Several ASO techniques have been developed in recent years [6]. ASO techniques can be broadly categorized into being either direct or surrogate-based [7]. Direct optimization (DO) techniques include gradient-based search (e.g., steepest descent, and sequential quadratic programming [8]) and derivative-free search (e.g., heuristic algorithms, such as genetic algorithms [9], or pattern search [7]). Derivative-free approaches typically require multiple model evaluations. Gradient-based search is the most widely adopted approach to solve ASO problems. ASO with gradient-based search algorithms was first attempted by Hicks and Henne back in the mid 1970's [10]. They developed numerical optimization algorithms for the design of subsonic and transonic airfoils and wings. The simulation models used in their studies were state-of-the-art at that time, but are now considered as low-fidelity methods. The derivatives were calculated using finite difference methods. In 1988, Jameson introduced adjoint sensitivity to ASO [11]. This technology transformed ASO as it enabled the calculation of the derivatives independent of the number of design variables. Gradient-based search using adjoint sensitivities is currently the state-of-the-art for ASO, see, e.g., [12].

Surrogate-based optimization (SBO) [13–15] is another way of performing ASO. The basic idea behind SBO is to replace the direct optimization of the computationally expensive model with an iterative process that involves the construction, optimization, and updating of a fast surrogate model [7]. Surrogates models can be broadly divided into two categories: data-fit surrogates, and multifidelity models [7, 16, 17]. Data-fit surrogates (also called approximation surrogates or metamodels) are constructed by approximating sampled high-fidelity model data using techniques such as polynomial approximation [14], kriging [18, 19] and neural networks [20]. In order to enhance the surrogate at global modeling accuracy or global optimum locating accuracy, numerous methods for allocating additional training points have been developed [15]. According to the work of Forrester and Keane [15], SBO with data-fit surrogates can be used as an efficient global optimization technique.

A multifidelity model is constructed by adapting or enhancing a low-fidelity model [21, 22]. The low-fidelity model can be obtained by either using simplified governing equations or exploiting the high-fidelity model with a coarser computational description [21, 23] and relaxed convergence criteria [23]. The low-fidelity model is subsequently adapted or enhanced to become a reliable representation of the high-fidelity model within the optimization run. In the

data-fit surrogate approach, a large amount of data samples is needed to ensure a decent accuracy. The multifidelity models contain information on the underlying physics through the low-fidelity model. Consequently, multifidelity models require less high-fidelity information to set up. Typically, the high-fidelity model is evaluated only once per design iteration. Forrester et al. [24, 25] developed multifidelity metamodel for the kriging response surface to fuse information from multi-level physics-based simulation models, and demonstrated the advantage of multifidelity modeling on computational cost and accuracy using aerodynamic wing design cases. Bryson and Rumpfkeil [26–28] developed a new unified multifidelity optimization approach based on quasi-Newton algorithm, which was integrated with polynomial and kriging models and was shown to be more computational efficient than direct optimization and trust-region model management method.

Over the last few decades, various adaptation techniques and related optimization algorithms have been developed, including the approximation and model management optimization (AMMO) [21], multipoint correction techniques [29, 30], several variations of output space mapping (SM) [29], as well as manifold mapping (MM) [31, 32]. Apart from the aforementioned ones, which are all so-called parametric methods [22] (where the adaptation functions are given explicitly with the parameters usually obtained by explicit calculations or solving auxiliary linear regression problems), a number of non-parametric technique have been developed, such as the shape-preserving response prediction (SPRP) [33], adaptive response correction (ARC) [34], and the adaptive response prediction (ARP) [35].

Parametric methods are preferred by many due to their simplicity. Among these, MM [31, 32] seems to be one of the most interesting because of its capability to accommodate available high-fidelity model data accumulated during the optimization run, as well as having the potential to approximately satisfy the first-order consistency with the high-fidelity model upon the algorithm convergence. Moreover, MM is capable of handling vector responses [31], making it, potentially, a good candidate for multipoint design problems. MM, however, has not yet been applied to ASO.

The major contributions of this work are the first applications of MM [31] to single- and multipoint ASO problems with multifidelity computational fluid dynamics (CFD) models. The proposed technique is validated and characterized by applying it to benchmark design problems and compared to state-of-the-art gradient-based shape optimization with adjoint sensitivity information. The benchmark cases include two single-point airfoil design cases developed by the AIAA Aerodynamic Design Optimization Discussion Group* (ADODG), as well as a multipoint airfoil design problem which highlights a unique feature of the proposed approach of handling vector-valued responses. The benchmark cases have fewer than 25 designable parameters. The results demonstrate that MM with multifidelity CFD models outperforms the gradient-based optimization with adjoints for the considered cases. Numerous researchers have studied the single-point airfoil ADODG benchmark cases [36–47] as well as multipoint ASO cases [3, 48–52].

^{*}https://sites.google.com/view/mcgill-computational-aerogroup/adodg

The remainder of the paper is organized as follows. In Section II, the optimization methodology is described, including the problem formulation, and the optimization techniques utilized in the course of this study. Section III presents the results of the numerical applications of the proposed technique to transonic inviscid and viscous problems involving the design of two-dimensional airfoil shapes. Section IV concludes the paper.

II. Methods

In this section, the PDE-constrained optimization problem formulation is given, and the techniques to solve it are described. In particular, direct and surrogate-based methods are described. The direct methods include derivative-free and gradient-based approaches. The surrogate-based method described is the multifidelity modeling using manifold mapping.

A. Problem Formulation

The aerodynamic design problems considered in this work involve nonlinear constrained optimization of airfoil shapes in two-dimensional transonic flow. The flow simulations are performed using accurate, but computationally expensive, high-fidelity CFD models. The high-fidelity simulations are denoted here by **f**. In general, nonlinear constrained optimization problems can be formulated as

$$\mathbf{x}^* = \arg\min_{\mathbf{x}} H(\mathbf{f}(\mathbf{x})),\tag{1}$$

s.t.
$$\mathbf{g}(\mathbf{x}) \le 0$$
, $\mathbf{h}(\mathbf{x}) = 0$, $\mathbf{l} \le \mathbf{x} \le \mathbf{u}$,

where \mathbf{x} is the design variable vector of size $n \times 1$, \mathbf{x}^* is the optimized design vector of size $n \times 1$, H is a scalar valued objective function, $\mathbf{f}(\mathbf{x})$ is a $m \times 1$ vector with the figures of merit, $\mathbf{g}(\mathbf{x})$ is a $p \times 1$ vector with the inequality constraints, $\mathbf{h}(\mathbf{x})$ is a $q \times 1$ vector with the equality constraints, and \mathbf{l} and \mathbf{u} are the design variable lower and upper bounds, respectively, both vectors of the same size as \mathbf{x} . The vectors $\mathbf{f}(\mathbf{x})$, $\mathbf{g}(\mathbf{x})$, and $\mathbf{h}(\mathbf{x})$ are all obtained, or derived, from the computationally expensive PDE simulations.

In aerodynamic shape optimization, the high-fidelity simulation model \mathbf{f} calculates the figures of merit. For example, in the two-dimensional case, \mathbf{f} can be composed as $\mathbf{f}(\mathbf{x}) = [C_{l.f}(\mathbf{x}) \quad C_{d.f}(\mathbf{x}) \quad C_{m.f}(\mathbf{x}) \quad A(\mathbf{x})]^T$, where $C_{l.f}(\mathbf{x})$ is the high-fidelity non-dimensional lift coefficient, $C_{d.f}(\mathbf{x})$ is the high-fidelity non-dimensional drag coefficient, $C_{m.f}(\mathbf{x})$ is the pitching moment coefficient, and $A(\mathbf{x})$ is the airfoil cross-sectional area. The subscript f denotes the high-fidelity model. In the case of a drag minimization problem, the objective function in problem (1) is set as

$$H(\mathbf{f}(\mathbf{x})) = C_{d,f}(\mathbf{x}). \tag{2}$$

The inequality constraints are set as

$$g_1(\mathbf{x}) = C_{m.min} - C_{m.f}(\mathbf{x}) \le 0, \qquad g_2(\mathbf{x}) = A_{min} - A(\mathbf{x}) \le 0,$$
 (3)

where $C_{m.min}$ is a minimum allowable pitching moment coefficient, and A_{min} is a minimum cross-sectional area. The equality constraint is

$$h_1(\mathbf{x}) = C_{l,t} - C_{l,f}(\mathbf{x}) = 0, \tag{4}$$

where $C_{l,t}$ is a target lift coefficient set by the designer. Here, the angle of attack, α , is used as a dummy variable to find the target lift coefficient value. All the constraints are handled directly in the optimization process.

B. Direct Optimization

Direct optimization can be broadly categorized into derivative-free and gradient-based search approaches [22]. Methods of the derivative-free type are typically more costly than their gradient-based counterparts, but have the benefit of being more immune to numerical noise. The latter may be present while using CFD simulation models, especially with coarse CFD model discretization. Due to the availability of adjoint information [11], it is possible to perform direct gradient-based optimization of computationally expensive simulation models. Using this method, the cost of obtaining the gradients is almost equivalent to one flow solution for any number of design variables.

A flowchart of a generic direct optimization algorithm is shown in Fig. 1 and has the following main steps: (1) consider the initial design and evaluate the objective function in terms of the high-fidelity simulation model at this design with the constraints, (2) update the design variables and evaluate the objective function again using the high-fidelity model, save the current design if the constraints are met, try the next design if the termination criteria is not satisfied, and (3) repeat the loop until the termination condition is satisfied. Note that in most cases, the high-fidelity simulation has to be evaluated in order to obtain the constraint terms. Also, obtaining the adjoint solution is an additional cost incurred during an evaluation of the high-fidelity PDE simulation.

1. Gradient-based search

This work uses the sequential least squares programming (SLSQP) gradient-based algorithm [53] with adjoints for comparison with the optimization technique proposed in this work. SLSQP is a slight modification of the Lawson and Hanson's nonlinear least-squares solver and uses the Han–Powell quasi–Newton method along with a BFGS update of the B–matrix and an L1–test function in the step–length algorithm [53]. For this algorithm, the termination condition is set only on the objective function: $|H^{(i)} - H^{(i-1)}| < \varepsilon_H$. $H^{(i)}$ is the high-fidelity objective function value at i^{th} iteration and ε_H is a user defined tolerance and is set to a value of 10^{-7} for this study.

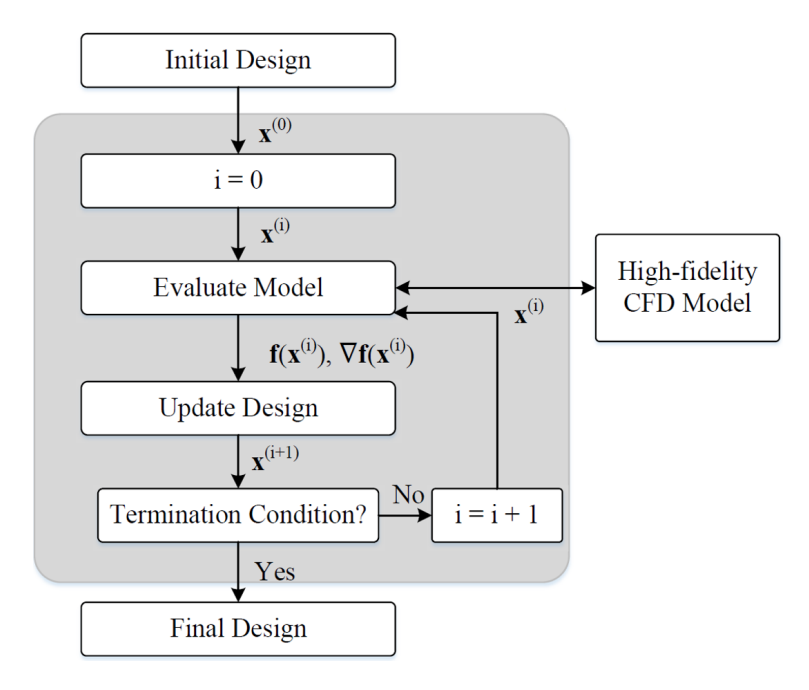


Fig. 1 A flowchart of the direct optimization algorithm.

2. Derivative-free search

Derivative-free search methods do not require gradient information, so it can be more immune to numerical noise than gradient-based approaches. Moreover, derivative-free methods can handle discontinuous functions better. However, in most cases, derivative-free algorithms require greater number of high-fidelity simulation evaluations to find the optimum than the gradient-based ones. Widely used global search include genetic algorithms (GAs) [54], and particle swarm optimization [55, 56]. For local search algorithms, the pattern search (PS) algorithm [54] is widely used.

We use the PS algorithm [54] in this work for (i) comparison purposes, and (ii) to drive our proposed multifidelity algorithm. The PS algorithm [54] is a stencil-based local optimization method that explores the neighborhood of the current design point. A rectangular grid (i.e., one point in each direction and in each dimension) is used in our implementation. The search process utilizes grid-constrained line search with the search direction determined using the objective function gradient estimated from perturbed designs. In case of a failure, the best perturbation (if better than the current design) is selected. Finally, the grid is refined in case the poll step does not lead to an improved design.

The details of PS algorithm are summarized as follows:

- 1) Evaluate objective function value, $H^{(i)}$, at current design, $\mathbf{x}^{(i)}$.
- 2) Evaluate objective function values, **H**, at perturbed designs, $\mathbf{x}^i + \mathbf{d}$, where $\mathbf{d} = (\mathbf{u} \mathbf{l})/10$.
- 3) Determine the search direction, $\mathbf{h} = -(\mathbf{H} H^{(i)})/\mathbf{d}$.
- 4) Normalize the direction for line search, $\mathbf{h} = |\mathbf{d}| * \mathbf{h} / |\mathbf{h}|$.
- 5) Run line search in loop
 - (a) Find the trial design $\mathbf{x}_{trial} = \mathbf{x}^{(i)} + \mathbf{h}$.

- (b) Adjust the trial design, following $\mathbf{x}_{tmp} = \mathbf{x}^{(i)} + round((\mathbf{x}_{trial} \mathbf{x}^{(i)}) \otimes \mathbf{d}) \circ \mathbf{d}$.
- (c) If objective function value at \mathbf{x}_{tmp} , $H(\mathbf{x}_{tmp}) < H^{(i)} : \mathbf{x}^{(i)} = \mathbf{x}_{tmp}$, $\mathbf{h} = 2 * \mathbf{h}$.
- (d) Otherwise, break the loop.
- 6) Start poll search in loop (maximum iteration = the dimension of random inputs), if line search failed
 - (a) Find the trial design $\mathbf{x}_{trial} = \mathbf{x}^{(i)}$.
 - (b) Adjust the trial design, following $\mathbf{x}_{tmp}(ceil(j/2)) = \mathbf{x}(ceil(j/2)) + ((-1)^j) * \mathbf{d}(ceil(j/2))$. If objective function value at \mathbf{x}_{tmp} , $H(\mathbf{x}_{tmp}) < H^{(i)}$: $\mathbf{x}_{min} = \mathbf{x}_{tmp}$.
 - (c) If poll search failed, reduce grid size as **d**/3.
 - (d) Otherwise, perform line search in the direction, $\mathbf{h} = \mathbf{x}_{min} \mathbf{x}^{(i)}$.

Find the trial design $\mathbf{x}_{trial} = \mathbf{x}^{(i)} + \mathbf{h}$.

Adjust the trial design, following $\mathbf{x}_{tmp} = \mathbf{x}^{(i)} + round((\mathbf{x}_{trial} - \mathbf{x}^{(i)}) \otimes \mathbf{d}) \circ \mathbf{d}$.

If objective function value at \mathbf{x}_{tmp} , $H(\mathbf{x}_{tmp}) < H^{(i)}$: $\mathbf{x}^{(i)} = \mathbf{x}_{tmp}$, $\mathbf{h} = 2 * \mathbf{h}$;

Otherwise, break the loop.

7)
$$\mathbf{x}^{(i+1)} = \mathbf{x}^{(i)}, H^{(i+1)} = H(\mathbf{x}^{(i)}).$$

Here, " \circ " is the Hadamard product of element-wise multiplication, " \odot " is Hadamard division of element-wise division, "round" forces the decimal to the nearest integer, "ceil" forces the decimal to the nearest integer in positive infinity direction. The PS algorithm is typically restarted using the last-step optimum until full convergence is reached. The termination conditions for this algorithm are: (i) norm of the design variables, $||\mathbf{x}^{(i)} - \mathbf{x}^{(i-1)}|| < \varepsilon_x$, or (ii) change in objective function, $|H^{(i)} - H^{(i-1)}| < \varepsilon_H$, where $\varepsilon_x = 10^{-6}$ and $\varepsilon_H = 10^{-7}$.

C. Multifidelity Optimization with Manifold Mapping

The basic idea of SBO is that the computation of the expensive high-fidelity simulation model is replaced by a series of fast surrogate models. A well-known approach for generating surrogate models is to sample the design space using design of experiments (DOE) [57–59] techniques, then evaluate the high-fidelity simulation at those designs and, subsequently, generate an approximation of the high-fidelity data using data-fit methods, e.g. Kriging interpolation [18]. The SBO algorithm updates the approximation by adding new high-fidelity information as it becomes available using infill criterion [15].

Multifidelity optimization follows the SBO paradigm. However, multifidelity models are constructed by adapting physics-based low-fidelity models [21, 22, 60]. A low-fidelity model, or a simplified description of the system under consideration, can be obtained by neglecting certain physical or second-order effects, using simplified equations, or by exploiting the high-fidelity model with a coarser computational description [21]. The low-fidelity models are subsequently adapted to become a reliable representation of the high-fidelity model by specific methods such as multiplicative or additive corrections [22], SM [29, 30], ARC [34], ARP [61], or SPRP [33].

Data-fit surrogates can be the basis of efficient global optimization techniques [15]. However, to ensure decent accuracy, data-fit surrogates require a large number of data samples. Moreover, the number of samples grows quickly with the problem dimensionality. Although the multifidelity models are not as versatile as the data-fit ones, they have the potential to offer significantly better efficiency in terms of the computational cost [21, 22, 60]. Many multifidelity algorithms require only a single high-fidelity model evaluation per design iteration [22]. Consequently, multifidelity models may exhibit better generalization capability than the approximation ones.

A flowchart of the multifidelity model-based optimization in Fig. 2 shows that the SBO process represented as [22]

$$\mathbf{x}^{(i+1)} = \arg\min_{\mathbf{x}} \mathbf{s}^{(i)}(\mathbf{x}),\tag{5}$$

where $\mathbf{x}^{(i)}$, i = 0, 1, ..., is a sequence of approximate solutions to the original problem (1), whereas $\mathbf{s}^{(i)}$ is the multifidelity model at iteration i. The multifidelity model should be cheap and accurate enough to represent the high-fidelity model, at least around the current design point, in the design space. Normally, the information from the high-fidelity model evaluation will be used in the next design iteration. Here, the computational time of the multifidelity model is very short. This may make the optimization process faster than direct optimization methods.

The key component of the multifidelity optimization algorithm is the physics-based low-fidelity (or coarse) model c embeds certain knowledge about the system under consideration, and allows us to construct a reliable multifidelity model using a limited amount of high-fidelity model data. In this work, the low-fidelity model is evaluated using the same CFD solver as the high-fidelity model f. Manifold mapping (MM) [32, 62] is considered as the adaptation method.

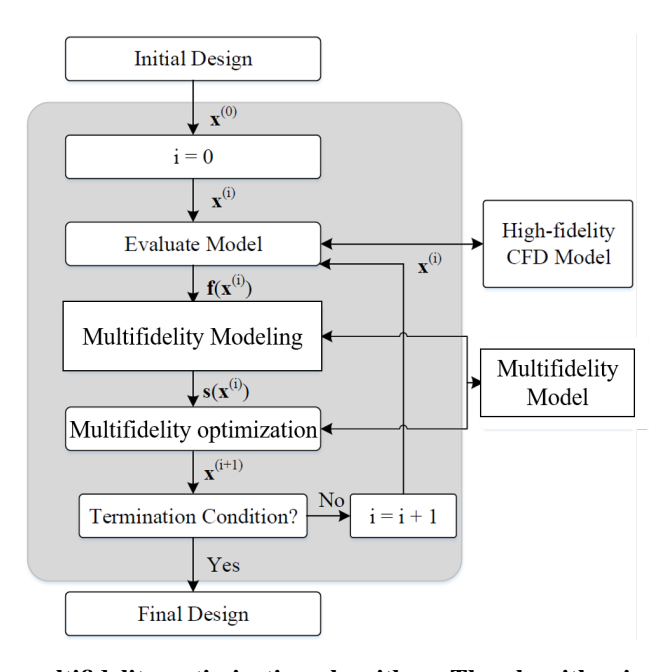


Fig. 2 A flowchart of the multifidelity optimization algorithm. The algorithm is embedded in a trust-region framework.

MM [31, 63] is a response adaptation technique that is capable of comprehensive exploitation of available high-fidelity model data. MM-based algorithms are local search methods and are typically embedded in a trust-region framework [64]. In this work, the PS [54] local search method is used to drive the optimization. In its basic version, the MM surrogate model is defined [31] as

$$\mathbf{s}^{(i)}(\mathbf{x}) = \mathbf{f}(\mathbf{x}^{(i)}) + \mathbf{S}^{(i)}(\mathbf{c}(\mathbf{x}) - \mathbf{c}(\mathbf{x}^{(i)}), \tag{6}$$

with $S^{(i)}$ being a 3 × 3 correction matrix in our case (in general, the size of S is equal to the number of the components in c, f, and s) defined as

$$\mathbf{S}^{(i)} = \Delta \mathbf{F} \cdot \Delta \mathbf{C}^{\dagger},\tag{7}$$

where

$$\Delta \mathbf{F} = [\mathbf{f}(\mathbf{x}^{(i)}) - \mathbf{f}(\mathbf{x}^{(i-1)}) \dots \mathbf{f}(\mathbf{x}^{(i)}) - \mathbf{f}(\mathbf{x}^{(max\{i-n,0\})})], \tag{8}$$

and

$$\Delta \mathbf{C} = [\mathbf{c}(\mathbf{x}^{(i)}) - \mathbf{c}(\mathbf{x}^{(i-1)}) \quad \dots \quad \mathbf{c}(\mathbf{x}^{(i)}) - \mathbf{c}(\mathbf{x}^{(max\{i-n,0\})})]. \tag{9}$$

The pseudo-inverse, denoted by †, is defined as

$$\Delta \mathbf{C}^{\dagger} = \mathbf{V}_{\Delta \mathbf{C}} \sum_{\Lambda \mathbf{C}}^{\dagger} \mathbf{U}_{\Lambda \mathbf{C}}^{T}, \tag{10}$$

where $\mathbf{U}_{\Delta \mathbf{C}}$, $\sum_{\Delta \mathbf{C}}$, and $\mathbf{V}_{\Delta \mathbf{C}}$ are the factors in the singular value decomposition of the matrix $\Delta \mathbf{C}$. The matrix $\sum_{\Delta \mathbf{C}}^{\dagger}$ is the result of inverting the nonzero entries in $\sum_{\Delta \mathbf{C}}$, leaving the zeros invariant [63].

The MM model alignment is illustrated in Fig. 3. Point \mathbf{x}_c^* denotes the minimizer corresponding to the low-fidelity model response, and the point \mathbf{y} is the vector of design specifications. Solid and dashed lines denote the tangent planes for the high- and low-fidelity model responses at their optimal designs. Upon convergence, the linear correction \mathbf{S}^* (being the limit of $\mathbf{S}^{(i)}$ with $i \to \infty$) maps the point $\mathbf{c}(\mathbf{x}^*)$ to $\mathbf{f}(\mathbf{x}^*)$, and the tangent plane for $\mathbf{c}(\mathbf{x})$ at $\mathbf{c}(\mathbf{x}^*)$ to the tangent plane for $\mathbf{f}(\mathbf{x})$ at $\mathbf{f}(\mathbf{x}^*)$.

It should be noted that although MM does not explicitly use sensitivity information, the multifidelity and the high-fidelity model Jacobians become more and more similar to each other towards the end of the MM-based optimization process (i.e., when $\|\mathbf{x}^{(i)} - \mathbf{x}^{(i-1)}\| \to 0$) so that the multifidelity model (approximately) satisfies both the zero- and first-order consistency conditions with \mathbf{f} . This allows for a more precise identification of the high-fidelity model optimum. On the other hand, the correction matrix $\mathbf{S}^{(i)}$ can be defined using exact Jacobians of the low- and high-fidelity models if available.

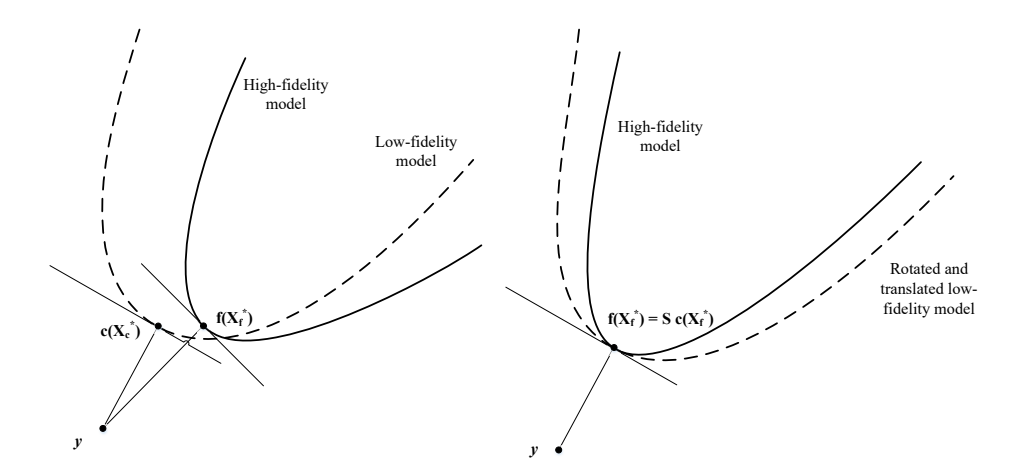


Fig. 3 A conceptual illustration of the manifold mapping model alignment (adapted and reproduced from Echeverria [31]).

In this work, the multifidelity optimization problem (5) is solved using the MM model (6) and driven by the PS algorithm [61] (Section II.B.2). The termination conditions are defined as: (i) norm of the design variables, $||\mathbf{x}^{(i)} - \mathbf{x}^{(i-1)}|| < \varepsilon_X$, or (ii) change in objective function, $|H^{(i)} - H^{(i-1)}| < \varepsilon_H$, or (iii) trust region radius, $\delta^{(i)} < \varepsilon_\delta$, with $\varepsilon_X = 10^{-6}$, $\varepsilon_H = 10^{-7}$, and $\varepsilon_\delta = 10^{-6}$.

III. Numerical Applications

In this section, the direct and multifidelity optimization algorithms are applied to three benchmark aerodynamic design problems involving inviscid and viscous transonic flow past airfoil shapes. Two of the cases were developed by the AIAA Aerodynamic Design Optimization Discussion Group (ADODG). The first two-dimensional case, Test Case I (TC I), is a single-point drag minimization of NACA 0012 in inviscid flow at zero lift, and the second case, Test Case II (TC II), is a single-point lift-constrained drag minimization of RAE 2822 in viscous flow. The third test case (TC III) is a multipoint variation of TC II. In particular, the case involves minimization of the weighted drag coefficients at several operating points subject to constraints.

A. Test Case I: Drag Minimization of the NACA 0012 Airfoil in Transonic Inviscid Flow

1. Problem definition

The objective is to minimize the drag coefficient (C_d) of the modified NACA 0012 airfoil section at a free-stream Mach number of $M_{\infty}=0.85$ and an angle of attack $\alpha=0$ deg subject to a minimum thickness constraint. The optimization problem is stated as:

$$\min_{\mathbf{l} \le \mathbf{x} \le \mathbf{u}} C_d(\mathbf{x}), \tag{11}$$

where \mathbf{x} is the vector of design variables, and \mathbf{l} and \mathbf{u} are the lower and upper bounds, respectively. The thickness constraint is stated as

$$y(x) \ge y(x)_{baseline},$$
 (12)

where y(x) is the airfoil thickness, $x \in [0, 1]$ is the chord-wise location, and $y(x)_{baseline}$ is the thickness of the baseline airfoil, which is a modified version of the NACA 0012, defined as

$$y(x)_{baseline} = \pm 0.6(0.2969\sqrt{x} - 0.1260x - 0.3516x^2 + 0.2843x^3 - 0.1036x^4).$$
 (13)

For the multifidelity algorithm, this thickness constraint (13) is handled through a quadratic penalty function, while for the derivative-free direct optimization algorithm, the pattern search algorithm is restricted to search within the feasible airfoil thickness region. For the gradient-based methods, the thickness constraint is implicitly satisfied by allowing the FFD control points to move only in the +y direction.

2. Design variables

The airfoil shape design variables are defined by the parametrization method. In this work, B-spline curves [65] as well as free-form deformation (FFD) [66] is used for the shape parametrization. Using B-spline curves the airfoil surfaces are written in parametric form as

$$x(t) = \sum_{i=1}^{n+1} X_i N_{i,k}(t), \tag{14}$$

and

$$y(t) = \sum_{i=1}^{n+1} Y_i N_{i,k}(t), \tag{15}$$

where (x, y) are the Cartesian coordinates of the surface, $N_{i,k}$ is the B-spline basis function of order k, (X_i, Y_i) are the coordinates of the B-spline control polygon, and n + 1 is the total number of control points. Note that the surface description with (14) and (15) is continuous.

For the FFD shape parameterization, Bézier curves are used to parameterize the airfoil geometry and are written as

$$\bar{\mathbf{X}}(u,v,w) = \sum_{i=0}^{l} \sum_{j=0}^{m} \sum_{k=0}^{n} P_{i,j,k} B_{i}^{l}(u) B_{j}^{m}(v) B_{k}^{n}(w), \tag{16}$$

where $P_{i,j,k}$ are the coordinates of the i, j and k control points. u, v and w are the parametric coordinates and lie in the interval [0,1]. l, m and n are the degrees of the FFD function and for this case is set to 24, 1 and 0, respectively. $B_i^l(u)$, $B_i^m(v)$ and $B_k^n(w)$ are the Bernstein polynomials. $\bar{\mathbf{X}}$ is the Cartesian coordinates of the airfoil surface.

The control points are used as design variables and allowed only to move freely vertically as shown in Fig. 4 (in this figure we only show the upper surface of the airfoil). For the B-spline case, 10 control points

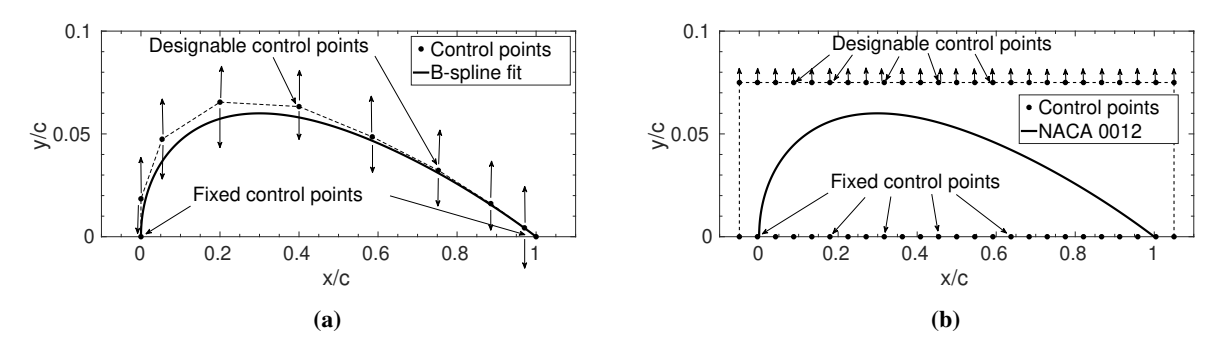


Fig. 4 Parameterization for the upper surface of the airfoil: (a) B-spline, (b) FFD.

are used as shown in Fig. 4, where two are fixed at the leading and trailing-edges, respectively, yielding 8 design variables in total. Based on a fit to the modified NACA 0012 of (13), we fix the x-locations of the free control points as $\mathbf{X} = [0, 0.0536, 0.2, 0.4, 0.5854, 0.7527, 0.8854, 0.9706]^T$. The initial design variable vector is $\mathbf{x}^{(0)} = [0.0185, 0.0474, 0.0654, 0.0633, 0.0486, 0.0323, 0.0161, 0.0043]^T$. The lower bound of \mathbf{x} is set as zero, i.e., $\mathbf{l} = \mathbf{0}$, and the upper bound is set as one, i.e., $\mathbf{u} = \mathbf{1}$. For the FFD case, 25 design variables are used and are uniformly distributed along the x-direction from -0.05 to 1.05. $\mathbf{x}^{(0)}$ is set to 0.075 for all the design variables. Lower bound $\mathbf{l} = \mathbf{x}$, in order to satisfy the thickness constraint. Upper bound $\mathbf{u} = \mathbf{1}$ for this case as well.

3. Aerodynamics modeling

The Stanford University Unstructured (SU2) computer code [67] version 6.2.0 is utilized for the inviscid fluid flow simulations. The steady compressible Euler equations are solved with an implicit density-based formulation. The convective fluxes are calculated using the second order Jameson-Schmidt-Turkel (JST) scheme [68]. The V-cycle multi-grid method [69] with three levels is used for solution acceleration. Asymptotic convergence to a steady state solution is obtained in each case. The flow solver convergence criterion is the one that occurs first of the two: (i) flow solution residuals fall below 10^{-10} , or (ii) a maximum number of iterations of 2,000 is met.

An O-type computational mesh is generated using the blockMeshDict utility in OpenFOAM [70] (see Fig. 5). Since the airfoil is symmetrical and the angle of attack is fixed at zero, only the half-plane is considered. The far-field boundary is set 55 chord lengths away from the airfoil surface. The mesh density is controlled by the number of cells on the airfoil surface and the number of cells normal to the surface. The results of a grid convergence study, given in Table 1, revealed that Mesh 5 converges to around 0.26 drag counts (1 drag count is defined as $\Delta C_d = 10^{-4}$) when compared with the next mesh. Distance to the first grid point is 0.0004c where c is the airfoil chord length. The flow simulation for Mesh 5 takes about 8.7 minutes. An adjoint solution for the drag coefficient takes approximately the same amount of time. It should be noted that throughout an optimization run, the airfoil shape may change significantly and the flow and adjoint simulation times may vary depending on the particular shape.

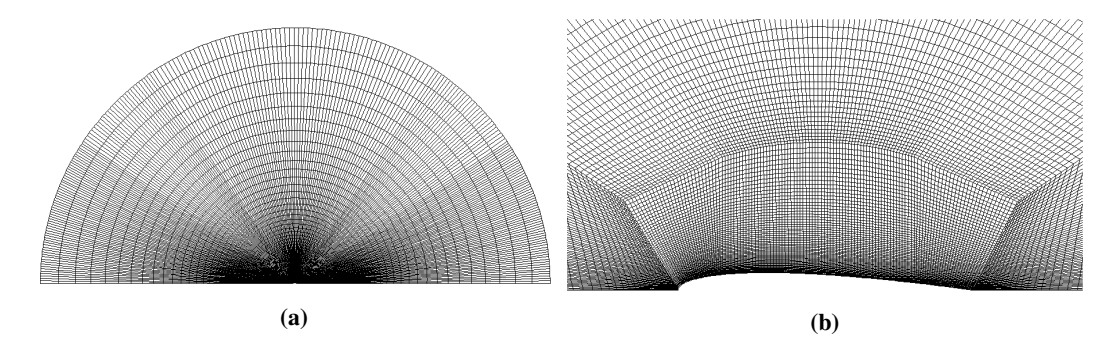


Fig. 5 Mesh views of half-plane O-mesh used in the inviscid model: (a) far field, (b) surface.

Table 1 Grid convergence study for the baseline shape of TC I at $M_{\infty} = 0.85$ and $\alpha = 0.0^{\circ}$.

Mesh	Grid Size	$\mathbf{C}_l(cts)$	$C_d(cts)$	Simulation Time (min)
1	1,720	0	525.48	0.22 *
2	6,862	0	489.78	0.3*
3	27,448	0	473.94	0.62*
4	109,792	0	469.66	1.82**
5	439,168	0	468.66	8.67**
6	1,756,672	0	468.40	46.10**

^{*}Computed on a high-performance cluster with 16 processors. Flow solution only.

For the optimization studies, Mesh 5 is used as the high-fidelity model \mathbf{f} , Mesh 3 with a new convergence criteria of either (i) change in absolute drag coefficient value over the last 100 iterations is less than 10^{-4} , or (ii) a maximum number of iterations of 1,000 is met, is used as the low-fidelity model \mathbf{c} . Figure 6 shows the solver convergence of the low-fidelity model. It also gives a comparison of the low- and high-fidelity model pressure coefficient profiles. Through this comparison, it can be seen that the low-fidelity model is a relatively good representation of the high-fidelity one.

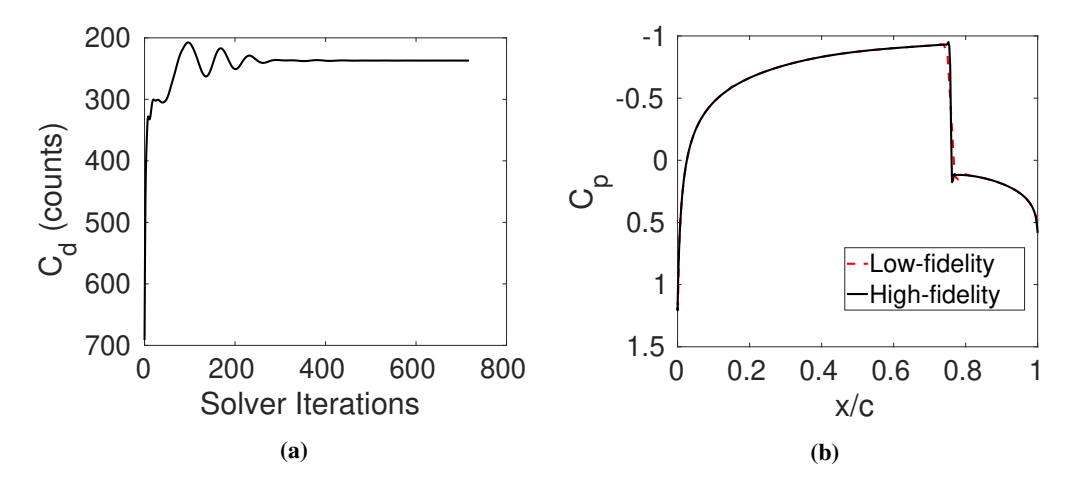


Fig. 6 Test case I CFD analysis of the initial design: (a) convergence history of the low-fidelity model, (b) pressure coefficient profile of the high- and low-fidelity models.

^{**}Computed on a high-performance cluster with 32 processors. Flow solution only.

4. Results

Table 2 gives the details of the optimization algorithms as well as their respective parameterization used for TC I. The MM approach uses a trust region method to find the optima, while the gradient-based approach uses the line search method. PS (HF) and PS (LF) refer to the cases, where the high- and low-fidelity models, respectively, are used to perform gradient-free optimization using the pattern search algorithm. Restart strategy refers to using the previous design iteration flow and adjoint field solution as an initial guess for the current design flow and adjoint field prediction, respectively. If restart strategy is not used, a uniform flow field is used as the initial guess. During the optimization process for the SLSQP cases, the mesh deformation module in SU2 [67] is used to update the shape and deform the mesh. For the PS and MM cases, the mesh is regenerated every time while updating the design.

Figure 7 shows that the gradients from adjoints match well with those from finite differences for the baseline geometry. Before optimizing this case using the SLSQP gradient-based optimizer, the gradients calculated using adjoints are compared to those from finite differences. The first-order forward difference approximation is used as the finite difference method and the step size is set to 10^{-4} .

Figure 8 shows the convergence of the argument \mathbf{x} and the evolution of the objective function H (here, the drag coefficient). For this case, the argument \mathbf{x} is not monitored for the gradient-based algorithms as the termination is only set on the objection function as mentioned in Section II.B. All the PS and MM cases terminate on \mathbf{x} .

Mesh for f Mesh for c Adjoints Trust Region Restart Strategy Parameterization Case Driver Algorithm PS (HF) Derivative-free Pattern Search 5 N/A N/A N/A No B-spline PS (LF) N/A N/A N/A B-spline Derivative-free Pattern Search No 3 MM Manifold Mapping Pattern Search 5 N/A Yes No B-spline 5 FFD SLSQP-1 Gradient-based **SLSQP** N/A Yes N/A No SLSQP-2 **SLSOP** FFD Gradient-based 5 N/A Yes N/A Yes

Table 2 Details of the optimization algorithms used for TC I.

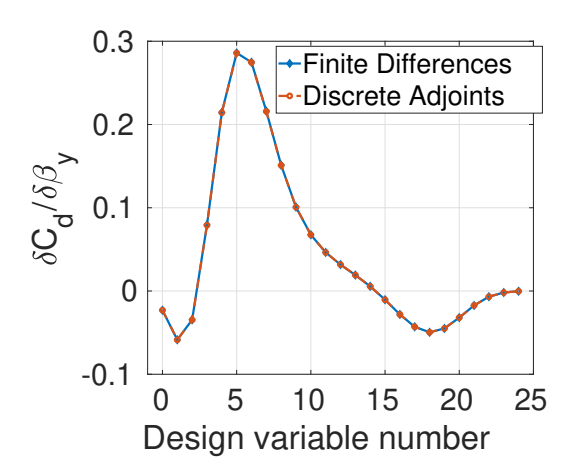


Fig. 7 Gradient comparison: adjoints v/s finite differences.

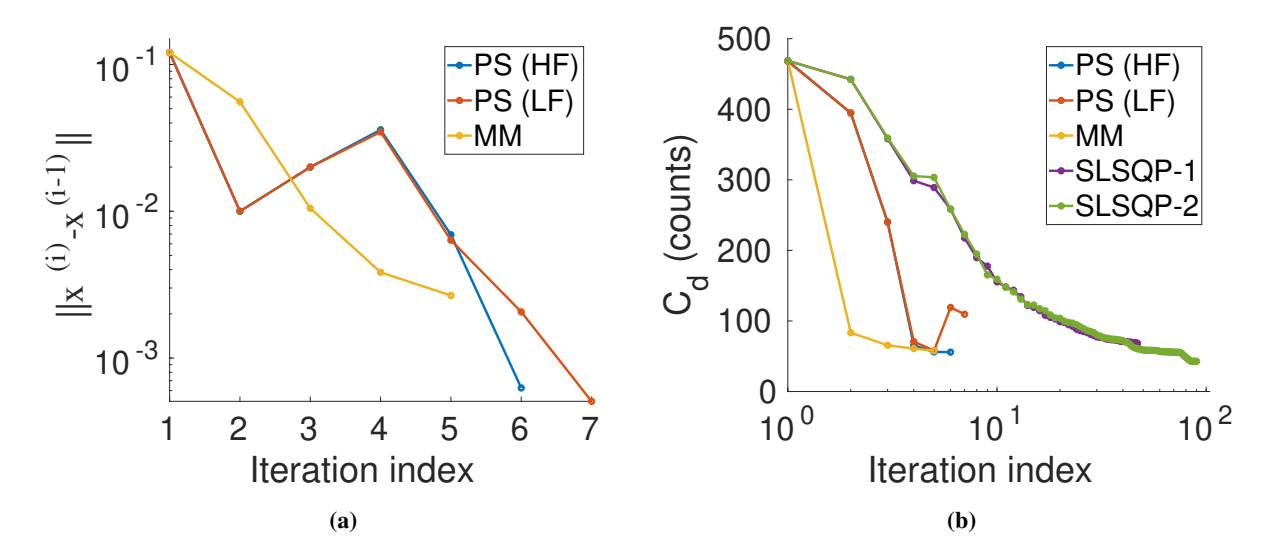


Fig. 8 TC I convergence history: (a) change in argument x, (b) objective function H.

In terms of design quality, the gradient-based algorithm with restart strategy (SLSQP-2) obtains the lowest drag coefficient value of 42.7 drag counts (Table 3). However, initializing with a uniform flow obtains a higher drag value of 68.3 drag counts (SLSQP-1). The MM algorithm is around two drag counts higher than the PS (HF) case. The PS (LF) case has the highest drag value of 109.1 drag counts. Note that in Fig. 8(b), the PS (LF) results are plotted by reevaluating the objective function with the high-fidelity model. The increase in drag coefficient value at iteration 6 is due to the poor prediction capabilities of the low-fidelity model at this design iteration. In this case, the low-fidelity model tricks the optimizer into finding a wrong optimum as well as increase the number of iterations.

Figure 9 shows the shapes obtained from the different cases and their corresponding pressure coefficients. Despite having similar shapes, the drag values are significantly different. The lower drag coefficient values are due to weaker shock strengths. All the shapes have reduced the shock strength significantly when compared to the baseline pressure distribution. Figure 10 shows the pressure coefficient contours for all the shapes, including the baseline.

Table 3 Optimization results for TC I.

Parameter/Method	Baseline	PS (HF)	PS (LF)	MM	SLSQP-1	SLSQP-2
$C_l(l.c.)$	0.0	0.0	0.0	0.0	0.0	0.0
$C_d(d.c.)$	468.66	55.76	109.14	57.86	68.28	42.75
N_c	-	-	1,408	1,036	-	0
N_f	-	1,058	-	5	120*	194*
$t_c(min)$	-	-	1,943	1,430	-	-
$t_f(min)$	-	8,178	-	39	1,783	1,536
$t_{tot}(min)$	-	8,178	1,943	1,469	1,783	1,536

^{*}Primary flow solutions as well as adjoint solutions.

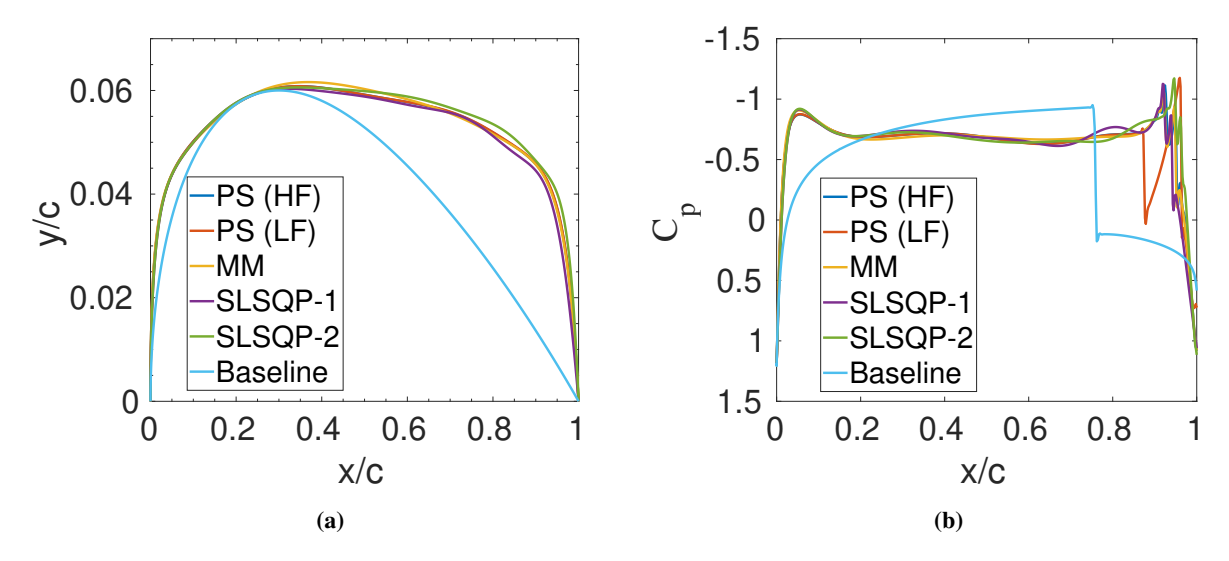


Fig. 9 Comparison of TC I baseline and optimized characteristics: (a) shapes, (b) pressure coefficient distributions.

In terms of computational cost, the MM algorithm needs the least amount of time. In particular, it requires five high-fidelity model evaluations (N_c), and 1,036 low-fidelity model evaluations (N_c). The total optimization time is about 1,469 minutes. PS (HF) and PS (LF) needed 8,178 and 1,943 minutes, respectively. SLSQP-2 needed a shorter time than SLSQP-1 despite requiring larger number of function evaluation. Using the flow field results from the previous design iteration provides a good initial guess of the current flow field results, leading to a decreased number of solver iteration to reach convergence, which in turn reduces the total computing time. Kedward et al. [37, 47] performed TC I using the gradient-based sparse nonlinear optimizer (SNOPT) with 8 B-splines control points and reached an optimum value of 52.5 drag counts. The total number of function evaluations reported were 51. This is significantly cheaper than those reported in Table 3. Kedward et al. [37, 47] also showed that increasing the number of B-spline control points to 64 reduced the optimum to 1.6 drag counts while increasing the number of function evaluations to 454. Similar trends were observed by He et al. [36] with the FFD parameterization and the SNOPT optimizer. They reported an optimum of 7.6 drag counts and a total number of iterations just below 1,000 (number of function evaluations not provided). The number of FFD control points used by He et al. [36] for this case was 25. The type of parameterization, as well as the position and number of design variables, affect the optimization performance significantly [43].

The restart strategy was used to analyze the issue of non-uniqueness reported for this case [36, 39]. The results are shown in Fig. 11. The optimum shape obtained from the SLSQP-2 case is reanalyzed with a uniform flow field and results in a significantly higher drag value of 108.1 drag counts. He et al. [36] also reported such results. They noticed an increase in drag to 109.9 drag counts from 7.6 drag counts while reanalyzing the case with a uniform flow field. The pressure coefficient profiles are the same for the two initialization strategies from the leading edge up to a chord length of 0.85c where the profiles differ significantly.

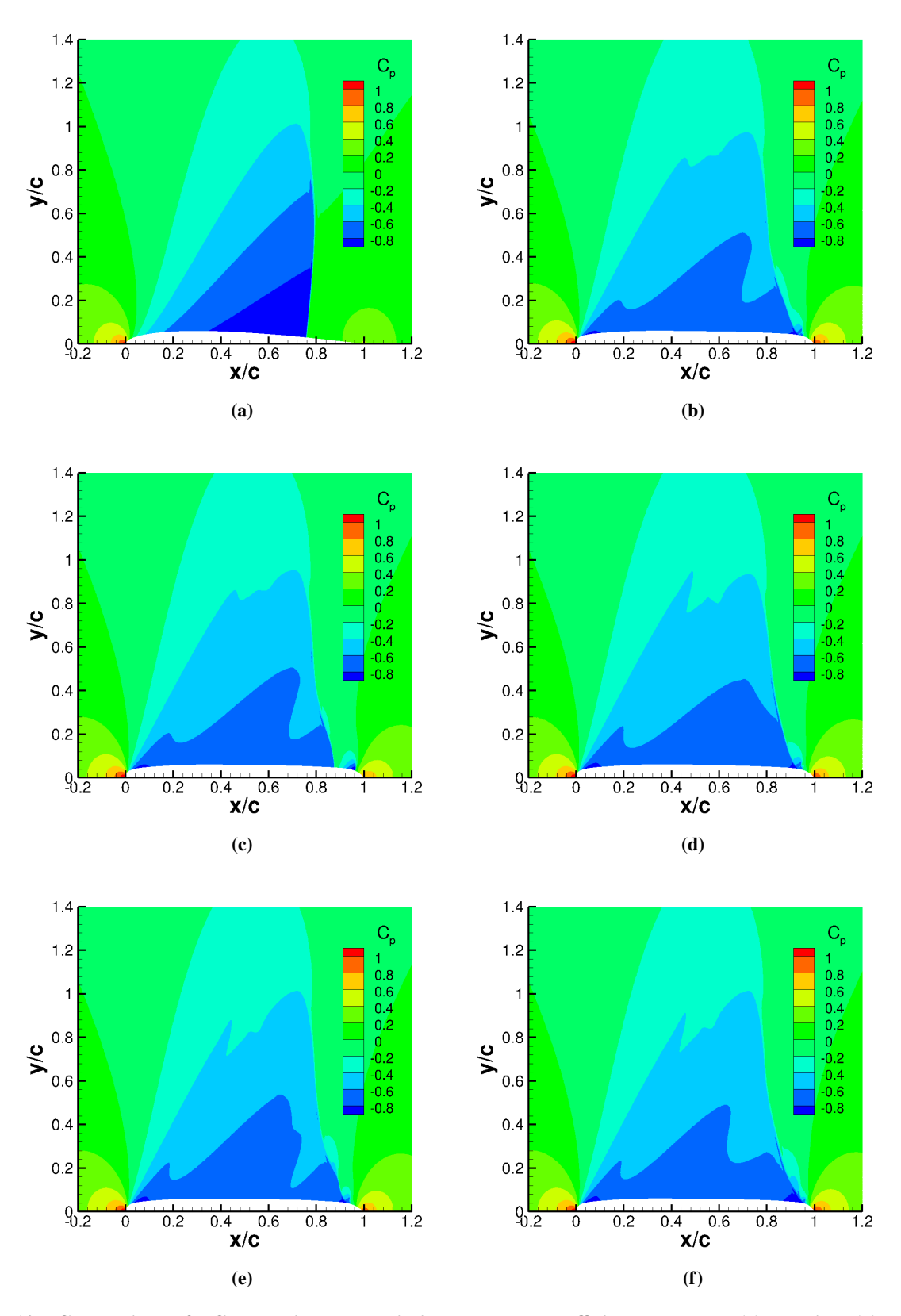


Fig. 10 Comparison of TC I baseline and optimized pressure coefficient contours: (a) baseline, (b) PS (HF), (c) PS (LF), (d) MM, (e) SLSQP-1, (f) SLSQP-2.

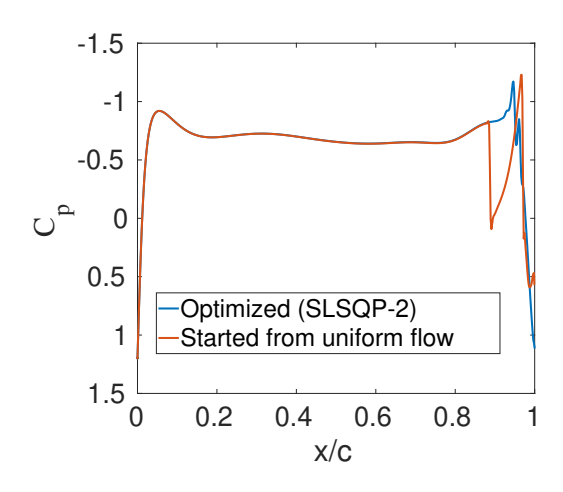


Fig. 11 Non-unique flow solution results.

Table 4 Grid convergence study for the optimized shape of TC I at M_{∞} = 0.85 and α = 0.0°.

Mesh	PS (HF)	PS (LF)	MM	SLSQP-1	SLSQP-2
1	334.4	335.1	338.82	338.82	329.58
2	127.64	126.12	125.98	124.9	153.74
3	66.56	115.06	68.32	78.38	117.3
4	57.44	106.8	59.29	70.23	111.94
5	55.76	109.14	57.86	69.10	108.06
6	55.54	108.72	57.54	68.94	100.44

Table 4 provides the results of the mesh convergence study on the optimized shapes obtained from the difference cases. All the cases, except for SLSQP-2, show a difference of around 0.2 drag counts between Meshes 5 and 6. For the SLSQP-2 case, this value is around eight drag counts. This analysis shows that Mesh 5 is a good high-fidelity model, aside from the SLSQP-2 case. Note that this mesh convergence study is performed using the same setup as that on the baseline shape.

B. Test Case II: Lift-constrained Drag Minimization of the RAE 2822 in Transonic Viscous Flow

1. Problem definition

The objective is to minimize the drag coefficient (C_d) of the RAE 2822 airfoil at a free-stream Mach number of $M_{\infty} = 0.734$, lift coefficient of 0.824, and Reynolds number of 6.5×10^6 , subject to an area and pitching moment constraints. The task is to solve the following constrained optimization problem:

$$\min_{\mathbf{l} \le \mathbf{x} \le \mathbf{u}} C_d(\mathbf{x}),\tag{17}$$

subject to the following constraints:

$$C_l(\mathbf{x}) = 0.824,\tag{18}$$

$$C_m(\mathbf{x}) \ge -0.092,\tag{19}$$

$$A(\mathbf{x}) \ge A_{baseline},$$
 (20)

where C_m is the moment coefficient, A is the airfoil cross-sectional area nondimensionalized with the chord length (c) squared, and $A_{baseline}$ is the nondimensionalized airfoil cross-sectional area of RAE 2822 and has a value of $0.07787c^2$.

The constant lift coefficient constraint (18) is implicitly satisfied in the flow solver by using the angle of attack as a dummy parameter. In the implementation of the multifidelity algorithms, the pitching moment and cross-sectional area constraints (19) and (20), respectively, are handled through a quadratic penalty function. In the derivative-free direct optimization algorithm, the pitching moment constraint is handled through a quadratic penalty function, while the area constraint is satisfied by restricting the pattern search algorithm to search within feasible airfoil area regions. For the gradient-based search algorithm, the Karush-Kuhn-Tucker (KKT) conditions are used to satisfy the constraint requirements.

2. Design variables

The B-spline and the FFD parameterization approaches, described in Section II.A, are used in TC II for the upper and lower surfaces. For the B-spline case, two different sets, with 10 and 18 control points, respectively, as shown in Fig. 12, where two are fixed at the leading- and trailing-edges, and the other ones, half for each surface, can move only in the vertical direction, are used in this study. This yields 8 and 16 design variables, respectively. Based on a fit to the RAE 2822, we set the *x*-locations of the free control points as $\mathbf{X} = [\mathbf{X}_u; \mathbf{X}_t]^T$. For the 8 variable case, $\mathbf{X} = [0.0 \ 0.15 \ 0.45 \ 0.80; \ 0.0 \ 0.35 \ 0.60 \ 0.90]^T$. For the 16 variable case, $\mathbf{X} = [0 \ 0.10 \ 0.20 \ 0.32 \ 0.45 \ 0.60 \ 0.75 \ 0.90; \ 0 \ 0.12 \ 0.25 \ 0.38 \ 0.50 \ 0.65 \ 0.78 \ 0.90]^T$. The initial design variable vector is $\mathbf{x}^{(0)} = [\mathbf{x}_u^{(0)}; \mathbf{x}_t^{(0)}]^T$. $\mathbf{x}^{(0)} = [0.0175 \ 0.0498 \ 0.0688 \ 0.0406; \ -0.0291 \ -0.0679 \ -0.0384 \ 0.0054]^T$ and $= [0.0185 \ 0.0420 \ 0.0535 \ 0.0635 \ 0.0656 \ 0.0622 \ 0.0432 \ 0.0205 \ -0.0203 \ -0.0480 \ -0.0557 \ -0.0685 \ -0.0553 \ -0.0287 \ -0.0126 \ 0.0040]^T$ for the 8 and 16 variables cases, respectively. The upper and lower bounds are set to $(1 \pm 0.25)\mathbf{x}^{(0)}$, respectively. The FFD case has 24 control points, 12 on the both the lower and upper sides of the airfoil as shown in Fig. 13. The control points are uniformly distributed along the *x*-direction from 0c and 1c. $\mathbf{x}^{(0)}$ for this case is set to 0.07 for all the control points on the upper side and -0.07 for all the control points on the lower side.

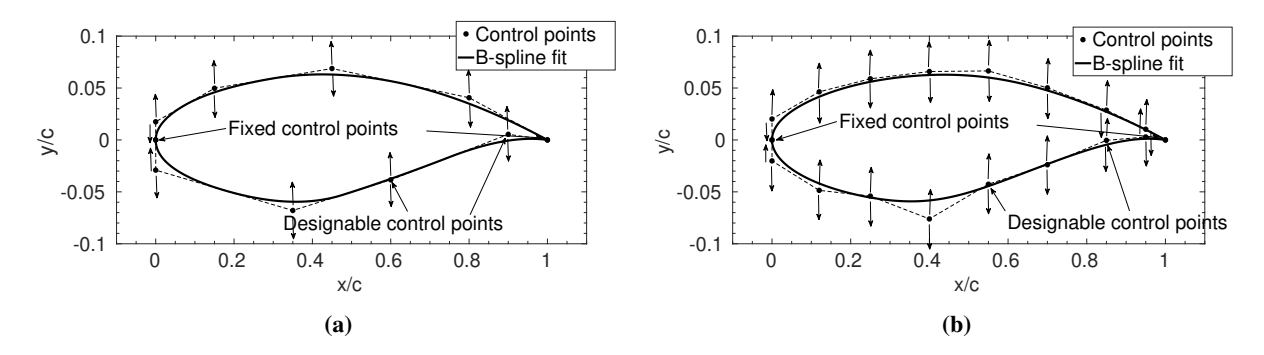


Fig. 12 B-spline parameterization for the surface of the airfoil: (a) 8 DV, (b) 16 DV.

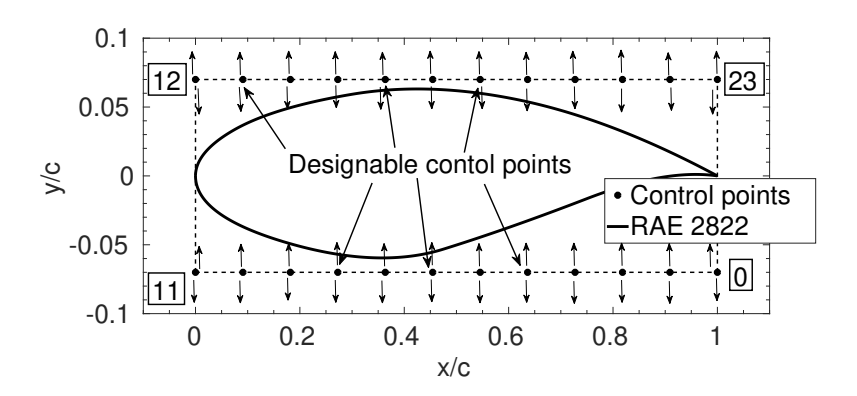


Fig. 13 FFD parameterization of the airfoil surface.

3. Aerodynamics modeling

The SU2 v7.0.0 implicit density-based flow solver [67] is used for the viscous case, solving the steady compressible Reynolds-averaged Navier-Stokes (RANS) equations with the Spalart-Allmaras turbulent model [71]. The convective flux is calculated using the second order JST scheme [68]. Three level V-cycle multi-grid [69] is used for solution acceleration. The turbulent variables are convected using a first-order scalar upwind method. The flow solver convergence criterion is the one that occurs first of the two: (i) flow solution residuals fall below 10^{-12} , or (ii) a maximum number of iterations of 20.000 is met.

An O-grid mesh is generated using the pyHyp code[†] (see Fig. 14). The far-field is set 55 chords away from the airfoil surface. The grid density is controlled by the number of points in the streamwise direction, and the number of points in the direction normal to airfoil surface. The first cell thickness is set to a value that ensures y^+ is less than one. Table 5 gives the results of a grid convergence study using the RAE 2822 airfoil at $M_{\infty} = 0.734$ and $C_l = 0.824$. The fixed C_l mode in SU2 is used to maintain the constant lift condition. Table 5 shows that Mesh 4 converges to 0.2 drag counts when compared to Mesh 5.

For the optimization studies, we use Mesh 4 for the high-fidelity model $\bf f$ and Mesh 2 for the low-fidelity model $\bf c$. Additionally, the low-fidelity model is limited to a maximum of 3,000 iterations. With this convergence criteria model $\bf c$

[†]https://github.com/mdolab/pyhyp

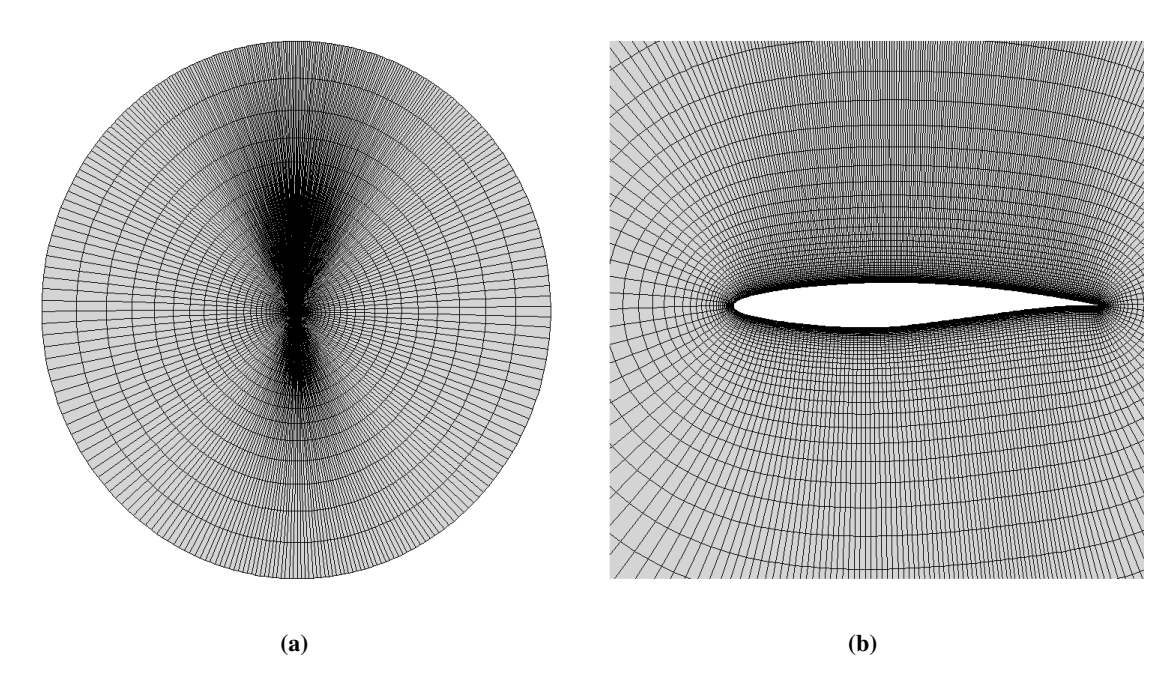


Fig. 14 Mesh views of hyperbolic O-mesh used in viscous model: (a) far field, (b) surface.

Table 5 Grid convergence study for the baseline shape of TC II.

Mesh	Grid Size	$\mathbf{C}_l(cts)$	$\mathbf{C}_d(cts)$	\mathbf{C}_m	Simulation Time * (min)
1	8,544	82.40	260.32	-0.0856	1.53
2	34,668	82.40	210.04	-0.0972	2.20
3	13,3536	82.40	201.93	-0.0985	7.38
4	525,096	82.40	200.57	-0.0984	48.35
5	2,082,216	82.40	200.78	-0.0980	831.38

^{*}Computed on a high-performance cluster with 64 processors. Flow solution only.

takes 1.5 minutes to simulate the flow past the baseline airfoil. Figure 15 shows the convergence of the low-fidelity solver and indicates that the low-fidelity model is a good representation of the high-fidelity one in terms of the pressure coefficient distribution for the baseline shape.

4. Results

An overview of the optimizers used in this case, along with their corresponding shape parameterization method and the number of design variables (N_{DV}), is given in Table 6. PS (HF) and PS (LF) refer to the cases which use the pattern search algorithm with the high- and low-fidelity models, respectively. The MM case is run with 8 and 16 B-spline control points, while the SLSQP case uses 24 control points of the FFD parameterization. Similar to TC I mesh deformation is used here for the SLSQP case while mesh regeneration is used for the PS and MM cases.

For the SLSQP approach, the gradients are calculated using adjoint information. Two adjoint simulations are needed, one for the objective function (drag coefficient) and the other for the pitching moment coefficient constraint. Gradients

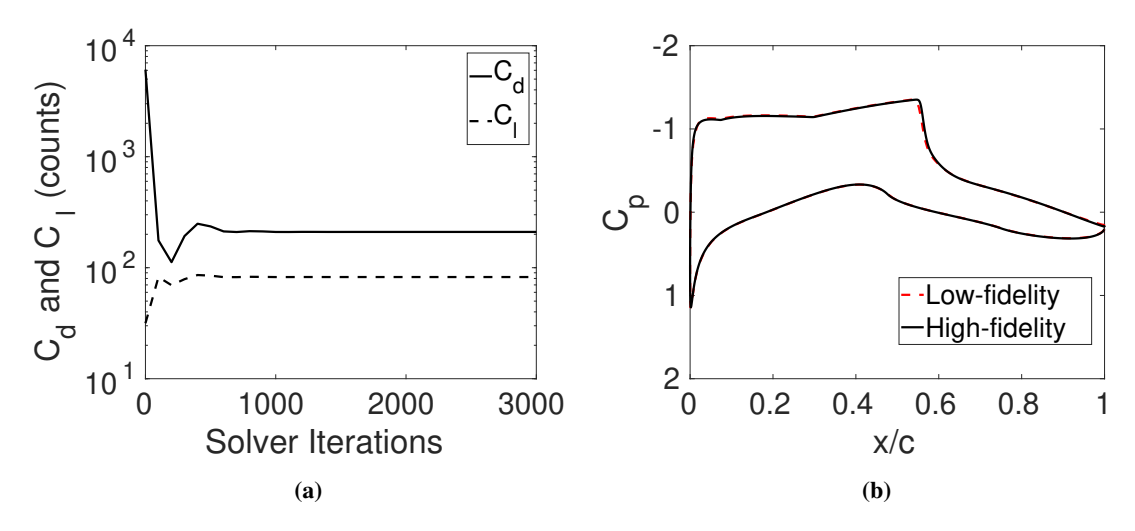


Fig. 15 Test case II CFD solver results at the baseline shape: (a) convergence history of the low-fidelity model, (b) pressure coefficient profile of the high- and low-fidelity models.

Table 6 Details of the optimization algorithms used for TC II.

Case	Algorithm	Driver	Mesh for f	Mesh for c	Adjoints	Trust Region	N _{DV}	Parameterization
PS (HF)	Derivative-free	Pattern Search	4	N/A	N/A	N/A	8	B-spline
PS (LF)	Derivative-free	Pattern Search	N/A	2	N/A	N/A	8	B-spline
MM-8DV	Manifold Mapping	Pattern Search	4	2	N/A	Yes	8	B-spline
MM-16DV	Manifold Mapping	Pattern Search	4	2	N/A	Yes	16	B-spline
SLSQP	Gradient-based	SLSQP	4	N/A	Yes	N/A	24	FFD

calculated from the adjoints for both the drag and pitching moment coefficients are validated by comparing them to those computed using first-order forward difference approximation of step size 10^{-5} and are shown in Fig. 16. The validation is done using Mesh 4 and on the baseline shape.

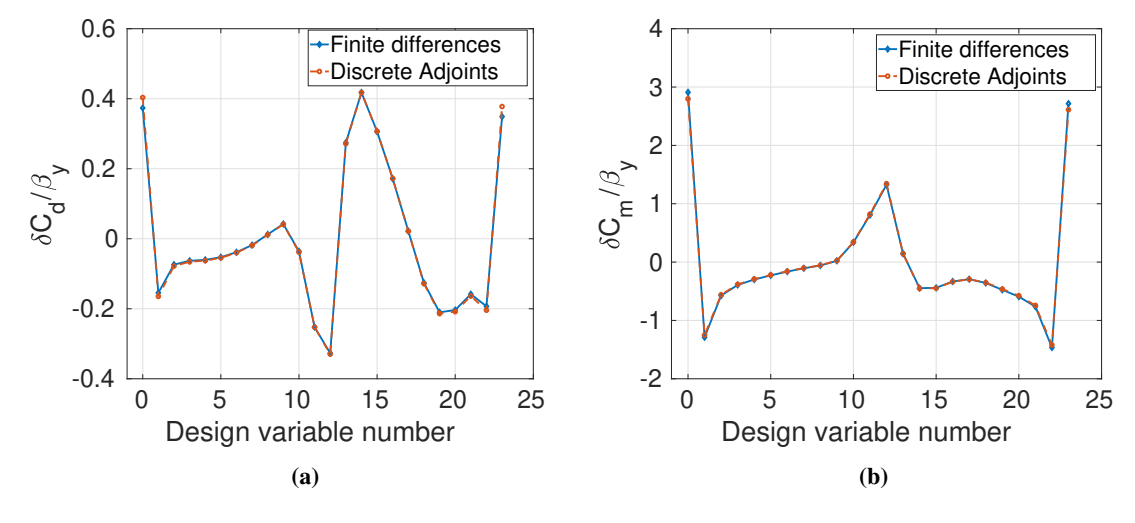


Fig. 16 Finite differences v/s discrete adjoints: (a) drag coefficient, (b) pitching moment coefficient.

Figure 17 shows the convergence history of the algorithms. The PS and MM-8DV cases terminate after two design iterations, while the MM-16DV case terminates after three. The MM and PS cases all terminate on the argument \mathbf{x} . The SLSQP case requires 45 design iterations and terminates on the objective function value. As was done for TC I, the PS (LF) run is reevaluated with the high-fidelity mesh and the results are plotted in Fig. 17(b).

Figure 18(a) compares the shapes obtained from the various optimizers with the baseline shape. Small differences are noticeable, but these small variations lead to large differences in the objective function values. Figure 18(b) shows the pressure distributions of the optimized shapes and the baseline. Figure 19 shows the pressure coefficient contours. The work done by He et al. [36] suggested that TC II has a global optimum and the results should be shock-free. Table 7

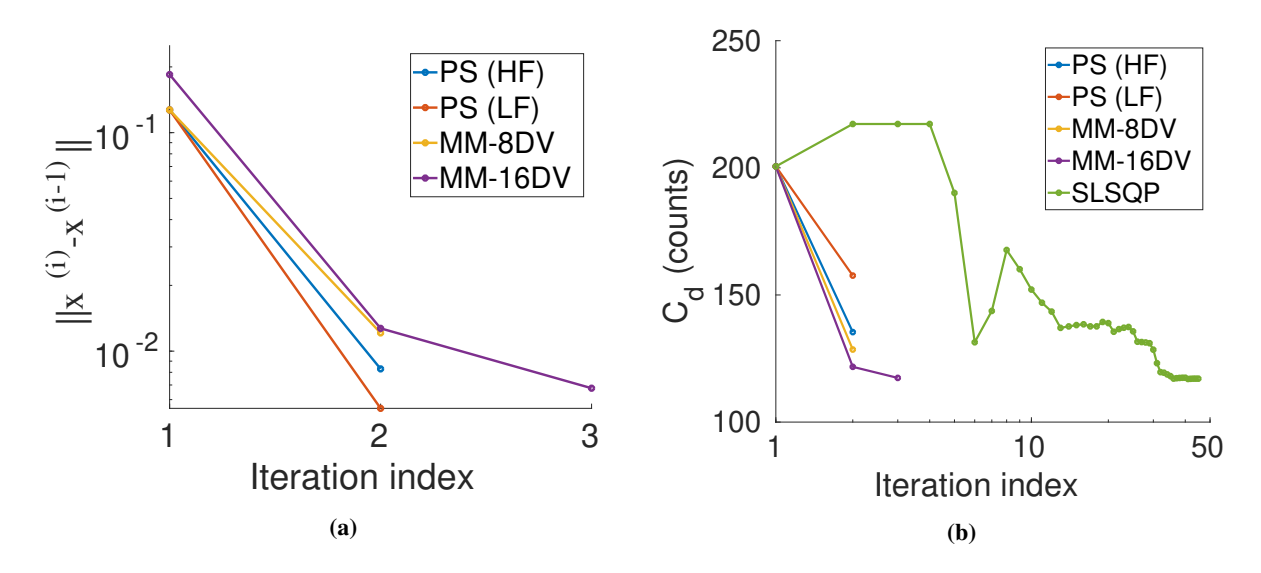


Fig. 17 TC II convergence history using MM: (a) change in argument x, (b) objective function.

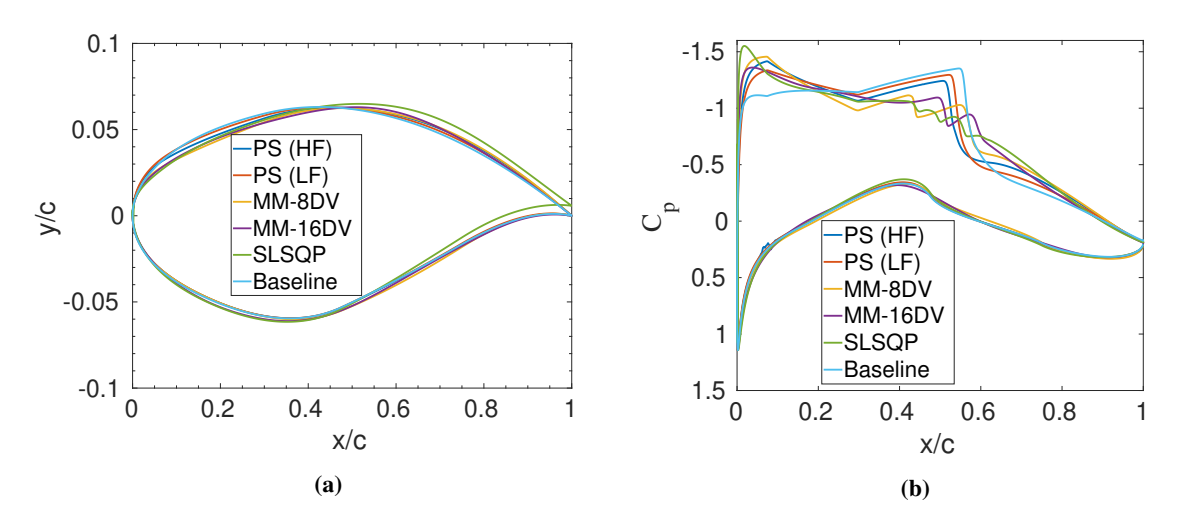


Fig. 18 TC II baseline and optimized shapes and pressure distributions: (a) shapes, (b) pressure coefficient distributions.

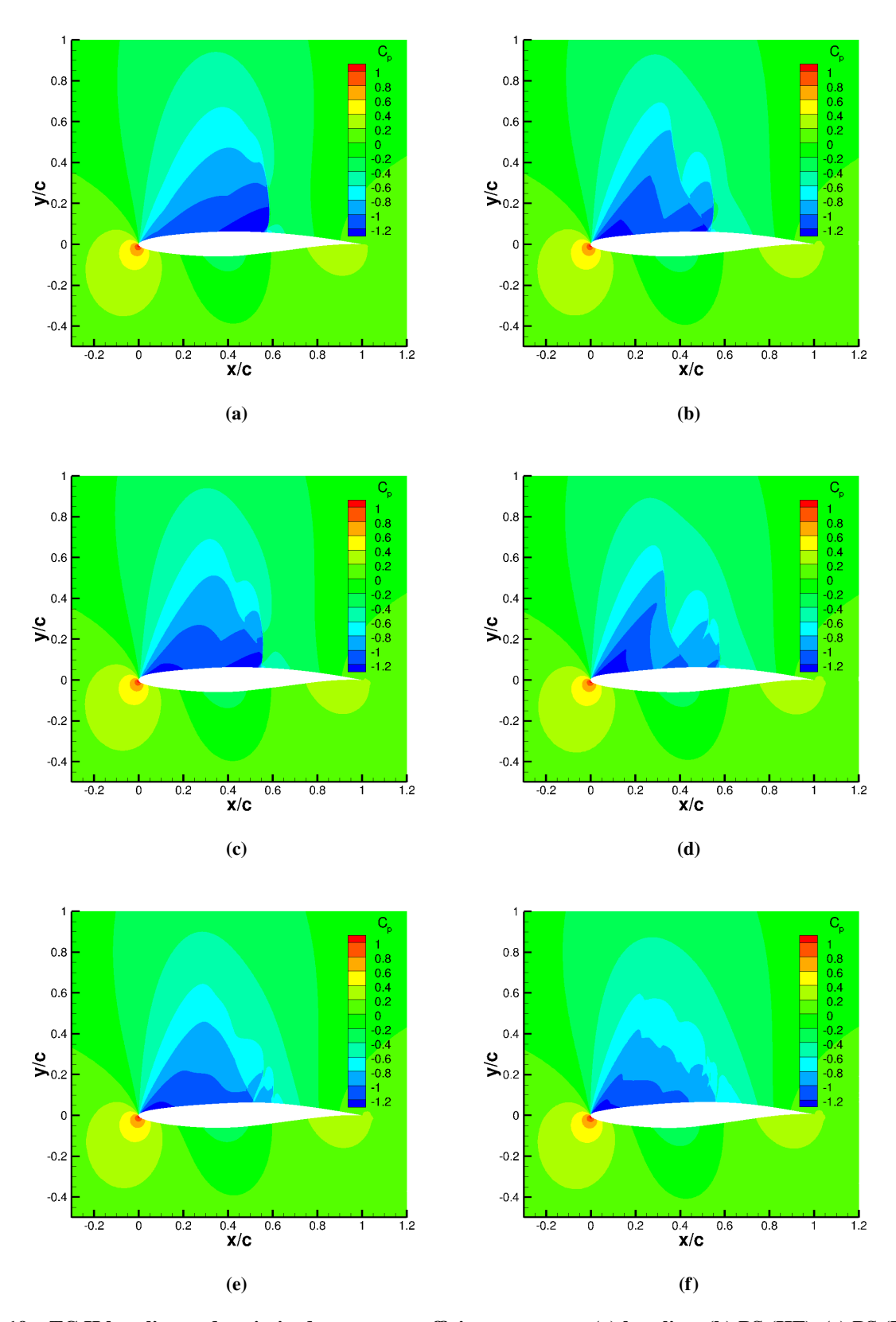


Fig.~19~TC~II~baseline~and~optimized~pressure~coefficient~contours:~(a)~baseline,~(b)~PS~(HF),~(c)~PS~(LF),~(d)~MM-8DV,~(e)~MM-16DV,~(f)~SLSQP.

Table 7 Optimization results for TC II.

Parameter/Method	Baseline	PS (HF)	PS (LF)	MM-8DV	MM-16DV	SLSQP
$C_l(l.c.)$	82.40	82.40	82.40	82.40	82.40	82.40
$C_d(d.c.)$	200.57	135.38	157.62	128.53	117.38	117.08
$C_{m,c/4}$	-0.0984	-0.0928	-0.0939	-0.0928	-0.0916	-0.0925
A	0.0779	0.0780	0.0780	0.0779	0.0782	0.0788
N_c	-	-	309	209	517	-
N_f	-	310	-	2	3	207*
$t_c(min)$	-	-	479	324	1,029	-
t_f (min)	-	19,759	-	100	227	10,350
t_{tot} (min)	-	19,759	479	424	1,256	10,350

^{*}Primary flow solutions as well as adjoint solutions.

shows that MM with eight design variables reduces the drag coefficient value from 200.6 counts to 128.5 counts (a reduction of 72.1 counts). This reduction is larger than both the PS cases. These three cases violate the pitching moment coefficient constraint and the solutions obtained are not shock free as seen in Fig. 18(b). A drag coefficient reduction of 83.2 drag counts is obtained for the MM-16DV case. This solution is still not shock free. The SLSQP case has the highest reduction in drag (83.4 drag counts), and the result is near shock-free. Lee et al. [38] and Bisson et al. [40] used SNOPT with 17 and 16 B-spline control points and obtained a shock-free solutions for this case. The *x*-locations of the control points are, however, not included in their work. Lee et al. [38] also used 7 and 9 B-spline control points for this case and did not obtain a shock-free solution. The lack of a shock-free solution can hence be attributed to the following reasons: low number of design variables, the optimization algorithm used to solve the problem, and the *x*-location of the design variables. Future work will examine the effects of these factors.

The MM-8DV case required 209 low-fidelity and 2 high-fidelity model evaluations to find the minimum. In terms of time, MM-8DV needs 424 minutes. PS (LF) requires slightly more time (479 min.), while PS (HF) required approximately 46 times that amount, MM-16DV case requires three times and SLSQP requires 24 times. Pattern search is known to scale poorly with the number of design variables, but for the MM algorithm, most of this cost is transferred to an increased number of low-fidelity model evaluations. This offsets some of the cost of increasing the number of design variables, improving the scalability of the pattern search algorithm. Lee et al. [38] required more than 610 model evaluations (flow plus adjoint) to find the optimum. Bisson et al. [40] required more than 120 model evaluations (number of minor iterations were not specified) to find the optimum. The MM-16DV case is hence significantly cheaper.

Table 8 shows the mesh convergence study on the optimized shapes for the different cases. Mesh 4 converges within 1.5 drag counts for all these cases when compared to Mesh 5. This shows that Mesh 4 performs well as a high-fidelity mesh. Note that the setup for this study is the same as the baseline shape mesh convergence study.

Table 8 Grid convergence study for the optimized shape of TC II.

Mesh	PS (HF)	PS (LF)	MM-8DV	MM-16DV	SLSQP
1	188.26	209.54	172.94	169.14	189.66
2	146.30	165.98	136.85	126.78	132.16
3	138.28	158.97	131.31	119.27	122.08
4	135.38	157.62	128.53	117.38	117.13
5	136.83	158.21	128.30	117.03	116.73

C. Test Case III: Multipoint Drag Minimization in Transonic Inviscid Flow

1. Problem definition

In TC III, three different multipoint cases are investigated. Like TC I and TC II, the idea of TC III comes from the ADODG benchmark case IV where the problem investigates the optimum solution for the common research model wing. Martins et al. [3, 48] has performed a lot of work on this benchmark case. In the present work, TC II is modified to perform multipoint optimization and the Euler equations are solved instead of the RANS equations to reduce computing time. This is done in order to focus on the performance of the MM algorithm. MM is compared to the gradient-based SLSQP algorithm.

The objective is to optimize the weighted sum of drag coefficients for several operation conditions. Comparison between multipoint design and single point design is performed. Case IIIa is the baseline single point optimization. The single point case and the new multipoint cases are summarized in Table 9. Figure. 20 shows the setup of the operational conditions of these designs. Cases IIIb and IIIc are multipoint cases. Case IIIb accounts for only varying Mach number while Case IIIc accounts for varying lift coefficient as well. The weight factors τ_i for these cases are shown in Table 9. The general form of each optimization problem can be described as follows.

Table 9 Operating conditions for each optimization cases.

Case	Point	Weights (τ_i)	Mach	C _l
IIIa	1	1	0.734	0.824
	1	$\frac{1}{4}$	0.724	0.824
IIIb	2	$\frac{1}{2}$	0.734	0.824
	3	$\frac{1}{4}$	0.744	0.824
	1	$\frac{1}{5}$	0.724	0.824
	2	$\frac{1}{5}$	0.734	0.774
IIIc	3	$\frac{1}{5}$	0.734	0.824
	4	$\frac{1}{5}$	0.734	0.874
	5	$\frac{1}{5}$	0.744	0.824

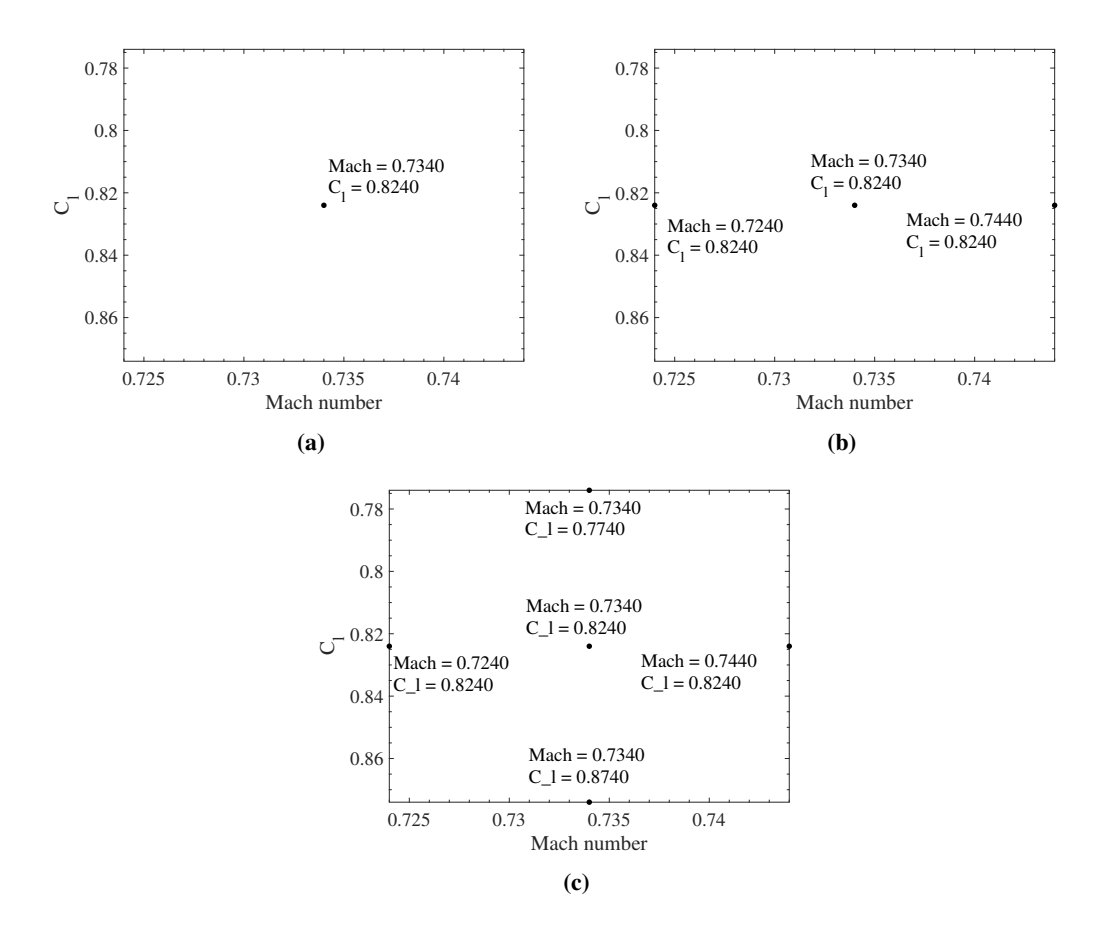


Fig. 20 TC III operational conditions of the singlepoint and multipoint designs: (a) Case IIIa, (b) Case IIIb, (c) Case IIIc.

The objective is to minimize the weighted average drag coefficient (\tilde{C}_d) subject to an area and lift coefficient constraint. The task is to solve the following constrained optimization problem:

$$\min_{1 \le \mathbf{x} \le \mathbf{u}} \sum_{i=1}^{N} \tau_i C_{di}(\mathbf{x}),\tag{21}$$

subject to

$$C_l(\mathbf{x}) = constant, \tag{22}$$

$$A(\mathbf{x}) \ge A_{baseline},$$
 (23)

where $A_{baseline}$ is the area of the RAE2822 airfoil. The constant lift coefficient constraint (22) values are listed in Table 9. The constraints for this case are managed in the way as TC II. The B-spline and FFD parameterization approaches, described in Section II.B, are used in this application as well. We use 8 control points for the B-spline (see Fig. 12) and 20 control points for the FFD (see Fig. 21).

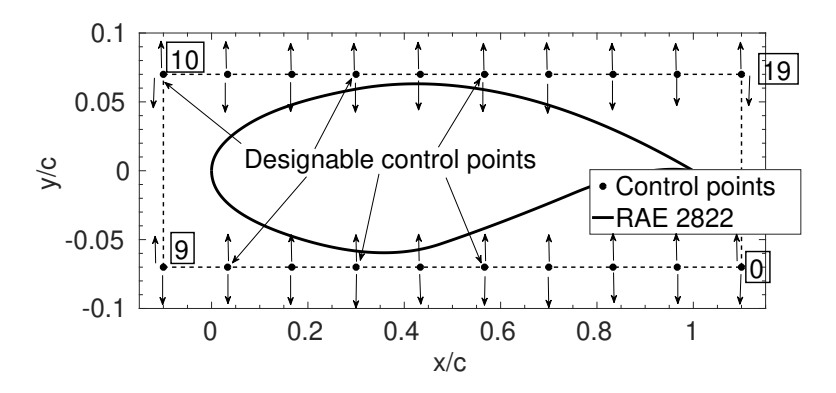


Fig. 21 FFD parameterization of the airfoil surface.

2. Aerodynamics Modeling

A similar mesh to TC II is generated for this case using pyHyp and is shown in Fig. 22. The only difference being that the first cell layer height is now increased to 0.0004c. The results of a grid convergence study, given in Table 10, revealed that Mesh 5 is converged within 0.21 drag counts of the finest mesh (Mesh 6). SU2 v7.0.0 is utilized for the inviscid fluid flow simulations [67]. The flow solver convergence criterion is the one that occurs first of the two: (i) flow solution residuals fall below 10^{-10} , or (ii) a maximum number of iterations of 5,000 is met. As with TC II, the fixed lift mode in SU2 is used to simulate the flow at constant lift.

For the optimization studies, we use Mesh 5 for the high-fidelity model \mathbf{f} and Mesh 2 for the low-fidelity model \mathbf{c} . The low-fidelity model convergence criteria is the same as the high-fidelity one, but with the maximum number of

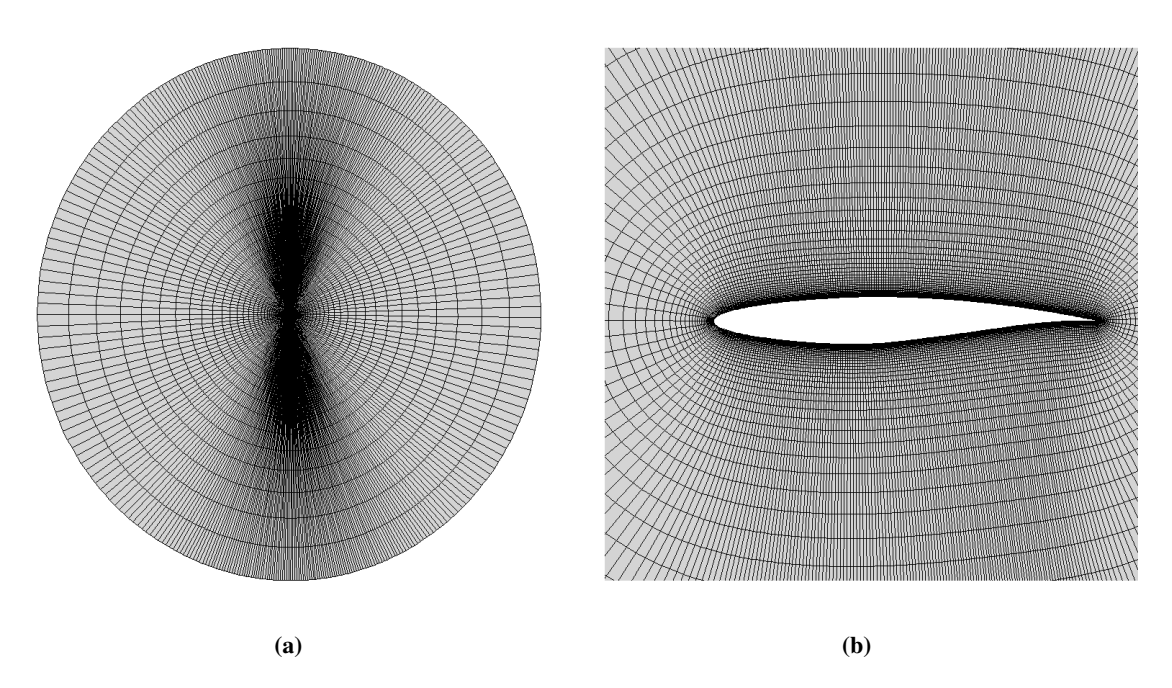


Fig. 22 O-mesh views of RAE 2822 airfoil: (a) far field, (b) surface.

Table 10 Grid convergence study for the baseline shape (RAE 2822).

Mesh	Grid Size	$\mathbf{C}_l(cts)$	$\mathbf{C}_d(cts)$	Simulation Time * (min)
1	1,764	82.4	231.82	0.3*
2	6,552	82.4	107.24	0.47*
3	25,752	82.4	82.68	0.9^{*}
4	101,618	82.4	77.93	2.1**
5	403,052	82.4	76.84	12.28**
6	1,606,518	82.4	76.63	65.77**

^{*}Computed on a high-performance cluster with 16 processors. Flow solution only.

^{**}Computed on a high-performance cluster with 32 processors. Flow solution only.

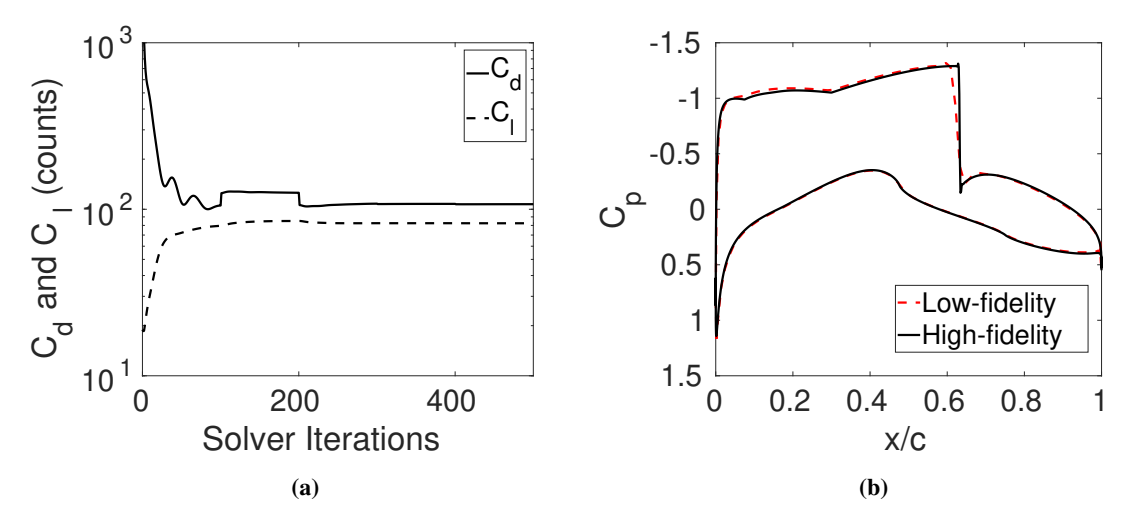


Fig. 23 Test case III CFD solver results at the baseline shape: (a) convergence history of the low-fidelity model, (b) pressure coefficient profile of the high- and low-fidelity models.

iterations limited to 500. The simulation time now reduces to 0.43 minutes. Figure 23(a) shows the convergence of the low-fidelity solver. Figure 23(b) shows that the low-fidelity model has a slight mismatch at the edge of shock on the upper surface with high-fidelity model. However, it is still a good representation of the high-fidelity model.

3. Results

The multipoint design cases are solved using both the MM as well as the SLSQP algorithms. Similar to the previous two cases, the MM algorithm uses pattern search as the optimization driver. For this case, mesh deformation is used for the SLSQP cases while mesh regeneration is used for the MM cases. For the SLSQP case, the gradients are calculated using discrete adjoints. To validate these gradients, they are compared to those calculated using first-order forward difference approximation with a step size of 10^{-5} . Figure 24 shows that these gradient values match well.

Figure 25 shows the optimized shapes for the MM and the SLSQP cases. The difference between the baseline and optimized shapes are not significant. The differences between optimized shapes are even less significant. However, the corresponding pressure distributions as seen in Fig. 26 vary considerably between the cases. Small changes in the

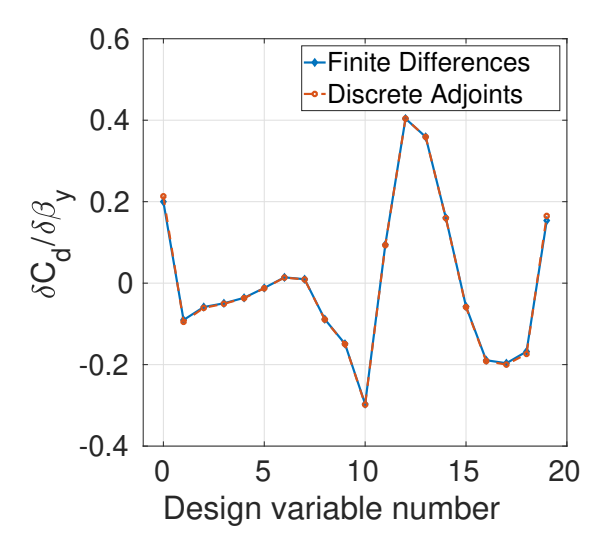


Fig. 24 Finite differences v/s discrete adjoints.

shapes can lead to large differences in the pressure distributions. Figure 26 shows that there are negligible differences in pressure coefficients for the MM results of Cases IIIb and IIIc.

Table 11 shows the optimized results for the three cases. In all three cases, a significant reduction in the objective function is achieved. In Case IIIa, MM obtains a slightly lower objective function value than SLSQP. For the remaining cases, SLSQP has a slightly higher reduction in the objective function value. MM requires significantly lower computing time when compared to the SLSQP cases. For Case IIIa it is approximately 3.5 times cheaper while for the other two cases it is more than ten times cheaper.

MM can handle vector responses [31] and the correction matrix $S^{(i)}$ improves in accuracy with increasing number

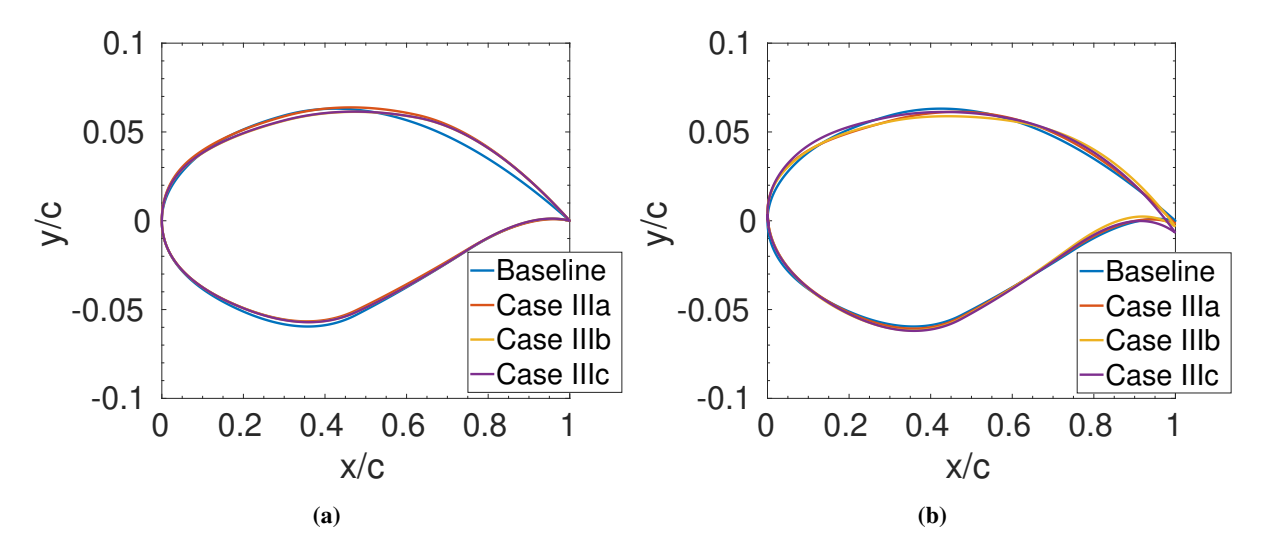


Fig. 25 Multipoint design baseline and optimized shapes: (a) manifold mapping, (b) SLSQP.

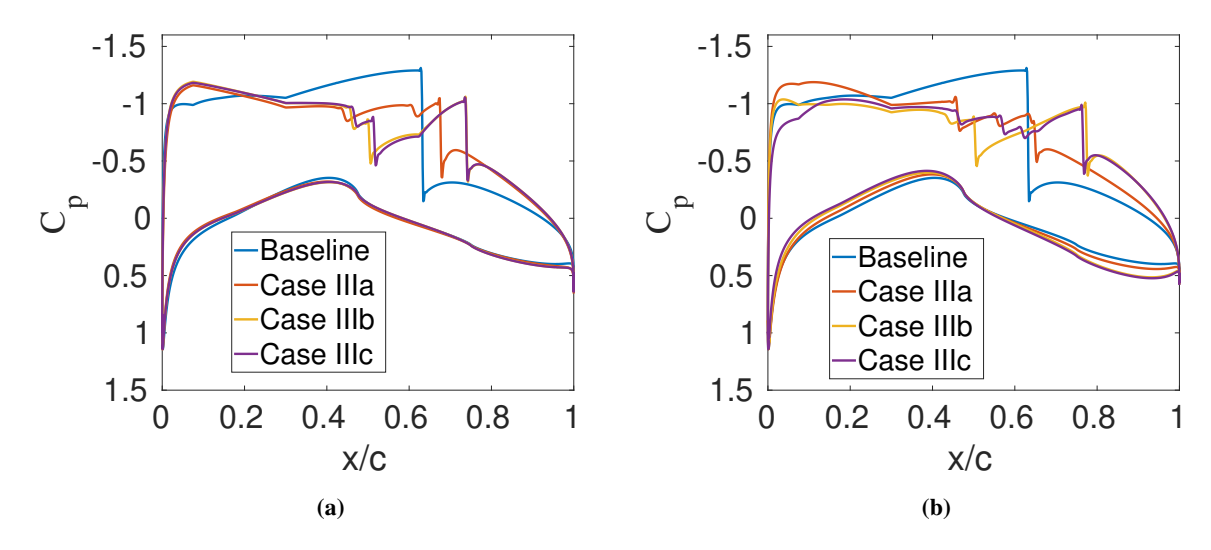


Fig. 26 Multipoint design baseline and optimized pressure coefficients: (a) manifold mapping, (b) SLSQP.

Table 11 Optimization results for TC III.

Parameter/Method	Case IIIa			(Case IIIb			Case IIIc		
1 al ameter/Method	Baseline	MM	SLSQP	Baseline	MM	SLSQP	Baseline	MM	SLSQP	
$ ilde{ ilde{C}_l(l.c.)}$	82.40	82.40	82.40	82.40	82.40	82.40	82.40	82.40	82.40	
$\tilde{C}_d(d.c.)$	76.84	12.02	12.21	79.24	15.59	12.13	80.22	15.97	13.31	
A	0.0779	0.0791	0.0779	0.0779	0.0779	0.0779	0.0779	0.0780	0.0800	
N_c	-	294	-	-	528	-	-	1,190	-	
N_f	-	2	33*	-	6	264*	-	10	440*	
$t_c \text{ (min)}$	-	126	-	-	227	-	-	512	-	
t_f (min)	-	32	528	-	100	4,224	-	164	7,040	
t_{tot} (min)	-	158	528	-	327	4,224	-	676	7,040	

^{*}Primary flow solutions as well as adjoint solutions.

of high-fidelity data (see (7)). For multipoint cases, each design iteration has multiple data points (three for Case IIIb and five for Case IIIc). This leads to more accurate surrogate models for multipoint cases when compared to single point. This in turn reduces the number of low-fidelity function evaluations N_c required to reach the minimum. In Table 11 the ratio of N_c between Cases IIIb and IIIa is 1.8 and between Case IIIc and IIIa it is four. The ratio of N_f for the same cases using the MM algorithm is three and five, respectively. For SLSQP, these ratios are eight and 13, respectively. MM hence has a lower cost per number of operating conditions for the multi-point cases, while SLSQP has a higher cost.

To explain the robustness of the multipoint design properly, we compare the ML/D contours with respect to C_l and Mach number for the baseline, single-point design (Case IIIa), and multipoint designs (Cases IIIa and IIIb). ML/D provides a metric for quantifying aircraft range based on the Breguet range equation with constant thrust-specific fuel consumption [3]. The higher the ML/D ratio, the longer the range. It is assumed the thrust-specific fuel consumption is constant in this case when performance falls into limited range of Mach number [72]. From Fig. 27, the maximum value

of ML/D of the baseline airfoil falls on a lower Mach number and a lower C_l than the nominal flight condition. The single-point optimization in Fig. 27 shows a movement of the optimum range of ML/D toward the nominal cruise condition. This is expected as the drag for this case was minimized for a fixed Mach number and C_l , thereby increasing the ML/D ratio. This ratio has also increased over the Mach number and C_l range when compared to the baseline case. The multipoint design in Fig. 28 shows a larger area of higher ML/D contours over the Mach number and C_l range when compared to the single point case (Fig.27). The decrease in ML/D ratio near the nominal conditions is more than compensated by the increase this this ratio over a wider range of Mach number and C_l , with Case IIIc having a wider area than Case IIIb. This shows the effect of performing multi-point optimization as compared to single-point optimization. The aircraft can now cruise over a longer distance for varying Mach number and C_l values.

Table 12 shows the grid independence study performed on all cases for TC III at nominal operating conditions and

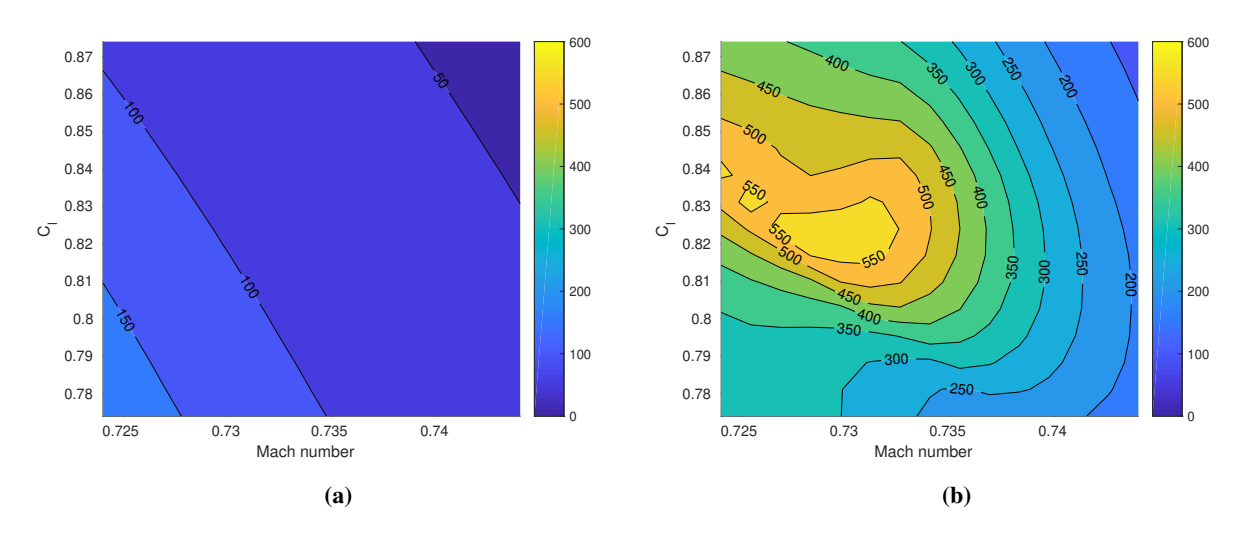


Fig. 27 Baseline and single point design ML/D contours (MM case): (a) baseline, (b) Case IIIa: single point.

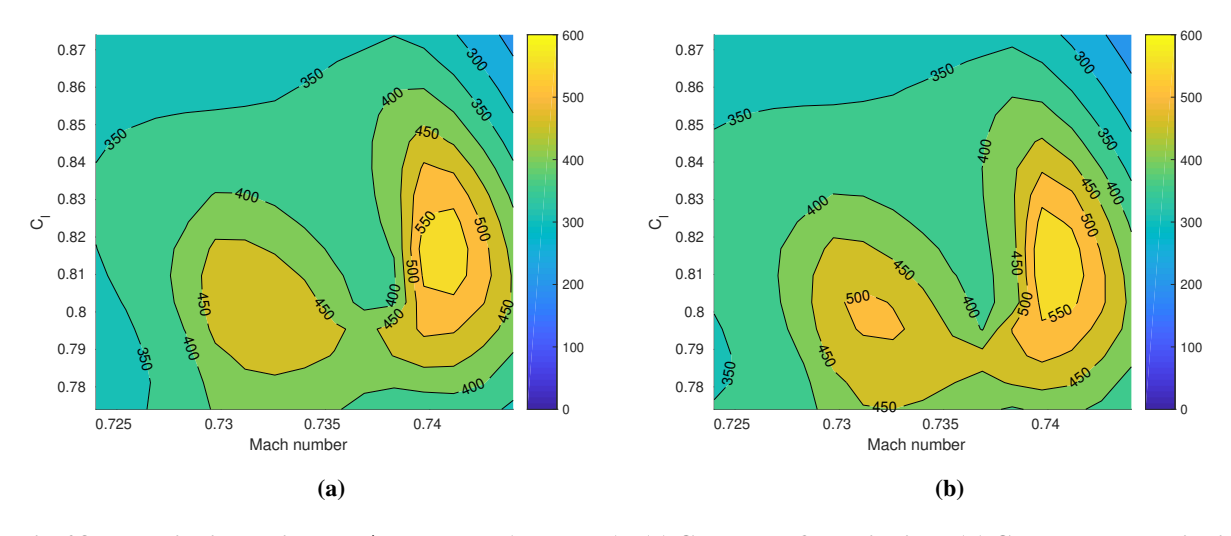


Fig. 28 Multipoint design ML/D contours (MM case): (a) Case IIIb: 3 multipoints, (b) Case IIIc: 5 multipoints.

Table 12 Grid convergence study for the optimized shape of TC III at nominal mach number.

Mesh -	Case	e IIIa	Case	e IIIb	Case IIIc		
	MM	SLSQP	MM	SLSQP	MM	SLSQP	
1	156.22	158.10	158.72	155.04	158.84	124.45	
2	35.98	43.43	39.36	39.99	39.08	30.76	
3	16.20	17.73	20.16	18.52	20.03	16.12	
4	12.80	13.18	16.23	14.34	16.29	12.54	
5	12.03	12.17	15.31	13.23	15.39	11.65	
6	12.04	12.11	15.26	13.13	15.35	11.72	

for the optimized shapes. The setup is the same as the baseline case and all the results for Mesh 5 have converged to less than 0.1 drag counts when compared to Mesh 6. Mesh 5 is therefore a good high-fidelity mesh.

IV. Conclusion

A robust and computationally efficient optimization algorithm for aerodynamic shape optimization (ASO) is presented. The approach uses low-fidelity models corrected locally by the manifold mapping (MM) technique to create fast and reliable multifidelity models which are utilized to search for an approximate optimum of an expensive high-fidelity model at a low CPU cost. The MM correction is applied both to the objectives and constraints to ensure a good alignment between the multifidelity model and the high-fidelity model at the current design point. The MM approach developed here does not require gradient information and requires only one high-fidelity model evaluation per design iteration. The approach is applied to benchmark cases involving direct design of airfoil shapes in two-dimensional inviscid and viscous transonic flows. As far is know from the literature, this is the first application of MM to ASO. Furthermore, it is the first application of MM to multipoint design optimization problems in general.

The performance of the MM algorithm was compared to the SLSQP gradient-based approach with the gradients calculated using adjoint sensitivity information. The MM method used B-splines to parameterize the geometry, while SLSQP used FFD. For both the benchmark cases, the optimum airfoil shapes are comparable with SLSQP resulting in slightly lower values of the objective function. On the other hand, SLSQP required more computational time compared to the MM approach. In particular, for TC I (inviscid flow past a symmetric airfoil at transonic speed) the computing time for SLSQP was slightly higher than MM but still comparable. For TC II (viscous flow past the RAE 2822 at a transonic speed and a constant lift coefficient), the computing time was significantly higher for SLSQP compared to MM. In fact in that case, SLSQP needed around one order of magnitude longer time to reach a comparable optimized shape as MM. It should be noted that the MM algorithm only used up to 16 design variables to solve the benchmark cases. The MM implementation presented in this work utilizes the pattern search algorithm to drive the optimization which is known to scale poorly with the number of design variables, whereas the gradient-based SLSQP with adjoints scales well.

Multipoint design optimization studies were also performed using MM and SLSQP approaches (TC III). MM was

originally developed to handle vector-valued responses. Multipoint ASO problems are examples of such cases. Here, the aerodynamic surface is optimized at multiple operating conditions, e.g., at several sets of Mach number and lift coefficients. The results show that the MM algorithm scales well with increasing number of multipoints, whereas the SLSQP with adjoints method scaled poorly. It was found that using the MM algorithm the multipoint cases could be solved at a computational cost which was around an order of magnitude lower than using SLSQP. SLSQP, however, resulted in slightly lower objective function values.

Future work will investigate alternatives to efficiently optimize the multifidelity model. In particular, extension of MM using adjoint sensitivity information will be investigated, as well as adding techniques for the reduction of the design space dimensionality. This will enable the use of MM for large-scale cases, e.g., the aerodynamic shape optimization of three-dimensional wings which may require several hundred design variables.

Acknowledgements

The first and fourth authors acknowledge the support of the National Science Foundation (NSF) award nr. 1846862. The fifth author acknowledges the support of the Icelandic Research Fund (RANNIS) award nr. 174573.

References

- [1] Kenway, G., and Martins, J. R. R. A., "Aerostructural Shape Optimization of Wind Turbine Blades Considering Site-Specific Winds," 12th AIAA/ISSMO Multidisciplinary Analysis and Optimization Conference, Victoria, British Columbia, Canada, September 10-12, 2008. doi:10.2514/6.2008-6025.
- [2] Mousavi, A., and Nadarajah, S., "Heat Transfer Optimization of Gas Turbine Blades Using an Adjoint Approach," 13th AIAA/ISSMO Multidisciplinary Analysis Optimization Conference, Fort Worth, Texas, Sep. 13-15, 2010. doi:10.2514/6.2010-9048.
- [3] Lyu, Z., Kenway, G. K. W., and Martins, J. R. R. A., "Aerodynamic Shape Optimization Investigations of the Common Research Model Wing Benchmark," *AIAA Journal*, Vol. 53, No. 4, 2015, pp. 968–984. doi:10.2514/1.J053318.
- [4] Nemec, M., Zingg, D. W., and Pulliam, T. H., "Multipoint and Multi-Objective Aerodynamic Shape Optimization," *AIAA Journal*, Vol. 42, No. 6, June, 2004, pp. 1057–1066. doi:10.2514/1.10415.
- [5] Jameson, A., Leoviriyakit, K., and Shankaran, S., "Multi-Point Aero-Structural Optimization of Wings Including Planform Variations," 45th Aerospace Sciences Meeting and Exhibit, Reno, Nevada, January 8–11, 2007. doi:10.2514/6.2007-764.
- [6] Fujii, K., and Dulikravich, G. S., *Recent Development of Aerodynamic Design Methodologies*, Vol. 65, Vieweg+Teubner Veriag, 1999.
- [7] Leifsson, L., and Koziel, S., Simulation-Driven Aerodynamic Design Using Variable-Fidelity models, Imperial College Press, London, UK, 2015.

- [8] Jacobs, J., Etman, L., Keulen, F., and Rooda, J., "Framework for Sequential Approximate Optimization," Structural and Multidisciplinary Optimization, Vol. 27, 2004, pp. 384–400. doi:10.1007/s00158-004-0398-8.
- [9] Foster, F. N., and G., D. S., "Three-Dimensional Aerodynamic Shape Optimization Using Genetic and Gradient Search Algorithms," *Journal of Spacecraft and Rockets*, Vol. 34, No. 1, January, 1997, pp. 36–42. doi:10.2514/2.3189.
- [10] Hicks, R. M., and Henne, P. A., "Wing Design by Numerical Optimization," *Journal of Aircraft*, Vol. 15, No. 7, 1978, pp. 407–412. doi:10.2514/3.58379.
- [11] Jameson, A., "Aerodynamic Design via Control Theory," Journal of Scientific Computing, Vol. 3, 1988, pp. 233–260. doi:10.1.1.419.9280.
- [12] Kim, S., Hosseini, K., Leoviriyakit, K., and Jameson, A., "Enhancement of Class of Adjoint Design Methods via Optimization of Parameters," *AIAA Journal*, Vol. 48, No. 6, 2010, pp. 1072–1076. doi:10.2514/1.42985.
- [13] Bandler, J. W., Cheng, Q. S., Dakroury, S. A., Mohamed, A. S., Bakr, M. H., Madsen, K., and Sondergaard, J., "Space Mapping: the State of Art," *Microwave Theory and Techniques, IEEE Transactions*, Vol. 52, No. 1, 2004, pp. 337–361. doi:10.1109/TMTT.2003.820904.
- [14] Queipo, N. V., Haftka, R. T., Shyy, W., Goel, T., Vaidynathan, R., and Tucker, P. K., "Surrogate-Based Analysis and Optimization," *Progress in Aerospace Sciences*, Vol. 41, 2005, pp. 1–28. doi:10.1109/TCPMT.2013.2285812.
- [15] Forrester, A. I. J., and Keane, A. J., "Recent Advances in Surrogate-Based Optimization," *Progress in Aerospace Sciences*, Vol. 41, No. 1–3, 2009, pp. 50–79. doi:10.1016/j.paerosci.2008.11.001.
- [16] March, A., and Willcox, K., "Provably Convergent Multifidelity Optimization Algorithm Not Requiring High-Fidelity Derivatives," *AIAA Journal*, Vol. 50, No. 5, 2012, pp. 1079–1089. doi:10.2514/1.J051125.
- [17] Rodriguez, J. F., Renaud, J. E., and Watsen, L. T., "Convergence of Trust Region Augmented Lagrangian Methods Using Variable Fidelity Approximation Data," *Structural Optimization*, Vol. 15, No. 3-4, 1998, pp. 141–156. doi:10.1007/BF01203525.
- [18] Kleijnen, J. P. C., "Kriging Metamodeling in Simulation: A Review," *European Journal of Operational Research*, Vol. 192, 2009, pp. 707–716. doi:10.1016/j.ejor.2007.10.013.
- [19] Jo, Y., and Choi, S., "Variable-Fidelity Aerodynamic Design Using Gradient Enhanced Kriging Surrogate Model with Regression," 52nd AIAA Aerospace Sciences Meeting, American Institute of Aeronautics and Astronautics, National Harbor, MD, 2014. doi:10.2514/6.2014-0900.
- [20] Rayas-Sanchez, J. E., "EM-Based Optimization of Microwave Circuits Using Artificial Neural Networks: The State-of-the-Art," *IEEE Trans. Microwave Theory Tech*, Vol. 52, 2004, pp. 420–435. doi:10.1109/TMTT.2003.820897.
- [21] Alexandrov, N. M., Lewis, R. M., Gumbert, C. R., Green, L. L., and Newman, P. A., "Optimization with Variable-Fidelity Models Applied to Wing Design," 38th Aerospace Science Meeting and Exibit, Reno, NV, Jan. 2000. doi:10.2514/6.2000-841.

- [22] Koziel, S., Echeverria-Ciaurri, D., and Leifsson, L., "Surrogate-Based Methods" in S. Koziel and X. S. Yang (Eds.) *Computational Optimization, Methods and Algorithms, Series: Studies in Computational Intelligence*, Springer-Verlag, Berlin Heidelberg, 2011.
- [23] Leifsson, L., and Koziel, S., "Multi-Fidelity Design Optimization of Transonic Airfoils Using Shape-Preserving Response Prediction," *Procedia Computer Science*, Vol. 1, No. 1, 2010, pp. 1311–1320. doi:10.1016/j.jocs.2010.03.007.
- [24] Forrester, A. I., Sobester, A., and Keane, A. J., "Multi-Fidelity Optimization via Surrogate Modelling," *Proceedings of the Royal Society A: Mathematical, Physical and Engineering Sciences*, Vol. 463, No. 2088, 2007, pp. 3251–3269. doi:10.1098/rspa.2007.1900.
- [25] Keane, A. J., "Wing Optimization Using Design of Experiment, Response Surface, and Data Fusion Methods," *Journal of Aircraft*, Vol. 40, No. 4, 2003, pp. 741–750. doi:10.2514/2.3153.
- [26] Bryson, D. E., and Rumpfkeil, M. P., "Comparison of Unified and Sequential-Approximate Approaches to Multifidelity Optimization," 55th AIAA Aerospace Sciences Meeting, American Institute of Aeronautics and Astronautics, Grapevine, TX, 2017. doi:10.2514/6.2017-0131.
- [27] Bryson, D. E., and Rumpfkeil, M. P., "Aeroelastic Design Optimization using a Multifidelity Quasi-Newton Method," *56th AIAA Aerospace Sciences Meeting, American Institute of Aeronautics and Astronautics*, Kissimmee, Florida, January 2018. doi:10.2514/6.2018-0102.
- [28] Bryson, D. E., and Rumpfkeil, M. P., "A Multifidelity Quasi-Newton Method for Design Optimization," *AIAA Journal*, Vol. 56, No. 10, 2018, pp. 4074–4086. doi:10.2514/1.J056840.
- [29] Koziel, S., Cheng, Q. S., and Bandler, J. W., "Space Mapping," *IEEE Microwave Magazine*, Vol. 9, No. 6, Dec. 2008, pp. 105–122. doi:10.1109/MMM.2008.929554.
- [30] Koziel, S., and Leifsson, L., "Knowledge-Based Airfoil Shape Optimization Using Space Mapping," 30th AIAA Applied Aerodynamics Conference, New Orleans, Louisiana, Jun. 25-28, 2012. doi:10.2514/6.2012-3016.
- [31] Echeverria, D., "Multi-Level Optimization: Space Mapping and Manifold Mapping," Ph.D. thesis, Thomas Stieltjes Institute for Mathematics, 2007.
- [32] Koziel, S., and Echeverria-Ciaurri, D., "Reliable Simulation-Driven Design Optimization of Microwave Structures Using Manifold Mapping," *Progress in Electromagnetic Research B (PIER B)*, Vol. 26, 2010, pp. 361–382. doi:10.2528/PIERB10090202.
- [33] Koziel, S., and Leifsson, L., "Surrogate-Based Aerodynamic Shape Optimization by Variable-Resolution Models," *AIAA Journal*, Vol. 51, No. 1, 2013, pp. 94–106. doi:10.2514/1.J051583.
- [34] Koziel, S., and Leifsson, L., "Adaptive Response Correction for Surrogate-based Airfoil Shape Optimization," *30th AIAA Applied Aerodynamics Conference*, New Orleans, Louisiana, Jun. 25-28, 2012. doi:10.2514/6.2012-3121.

- [35] Koziel, S., and Leifsson, L., "Multi-Fidelity Airfoil Optimization with Adaptive Response Prediction," *14th AIAA/ISSMO/Multidisciplinary Analysis and Optimization Conference*, Indinanapolis, Indiana, Sep. 17-19, 2012. doi:10.2514/6.2012-5454.
- [36] He, X., Li, J., Mader, C. A., Yildirim, A., and Martins, J. R. R. A., "Robust aerodynamic shape optimization-From a circle to an airfoil," *Aerospace Science and Technology*, Vol. 87, 2019, pp. 48 61. doi:https://doi.org/10.1016/j.ast.2019.01.051.
- [37] Kedward, L., Allen, C. B., and Rendall, T., "Regularisation of High Fidelity Aerodynamic Shape Optimisation Problems Using Gradient Limits," *AIAA Aviation 2019 Forum*, Dallas, Texas, USA, June 17-21, 2019. doi:10.2514/6.2019-3175.
- [38] Lee, C., Koo, D., Telidetzki, K., Buckley, H., Gagnon, H., and Zingg, D. W., "Aerodynamic Shape Optimization of Benchmark Problems Using Jetstream," *53rd AIAA Aerospace Sciences Meeting*, Kissimmee, FL, January 5-9, 2015. doi:10.2514/6.2015-0262.
- [39] LeDoux, S. T., Vassberg, J. C., Young, D. P., Fugal, S., Kamenetskiy, D., Huffman, W. P., Melvin, R. G., and Smith, M. F., "Study Based on the AIAA Aerodynamic Design Optimization Discussion Group Test Cases," *AIAA Journal*, Vol. 53, No. 7, 2015, pp. 1910–1935. doi:10.2514/1.J053535.
- [40] Bisson, F., Nadarajah, S., and Shi-Dong, D., "Adjoint-Based Aerodynamic Optimization Framework," *52nd Aerospace Sciences Meeting*, National Harbor, Maryland, USA, January 13-17, 2014. doi:10.2514/6.2014-0412.
- [41] Anderson, G. R., Nemec, M., and Aftosmis, M. J., "Aerodynamic Shape Optimization Benchmarks with Error Control and Automatic Parameterization," *53rd AIAA Aerospace Sciences Meeting*, *2015*, Kissimmee, FL, January 5-9, 2015. doi:10.2514/6.2015-1719.
- [42] Zhang, Y., Han, Z.-H., Shi, L., and Song, W.-P., "Multi-round Surrogate-based Optimization for Benchmark Aerodynamic Design Problems," 54th AIAA Aerospace Sciences Meeting, 2016, San Diego, CA, January 4-8, 2016. doi:10.2514/6.2016-1545.
- [43] Masters, D. A., Poole, D. J., Taylor, N. J., Rendall, T. C. S., and Allen, C. B., "Influence of Shape Parameterization on a Benchmark Aerodynamic Optimization Problem," *Journal of Aircraft*, Vol. 54, No. 6, 2017, pp. 2242–2256. doi:10.2514/1.C034006.
- [44] Carrier, G., Destarac, D., Dumont, A., Meheut, M., Din, I. S. E., Peter, J., Khelil, S. B., Brezillon, J., and Pestana, M., "Gradient-Based Aerodynamic Optimization with the elsA Software," *52nd Aerospace Sciences Meeting*, National Harbor, Maryland, USA, January 13-17, 2014. doi:10.2514/6.2014-0568.
- [45] Poole, D. J., Allen, C. B., and Rendall, T., "Control Point-Based Aerodynamic Shape Optimization Applied to AIAA ADODG Test Cases," *53rd AIAA Aerospace Sciences Meeting*, *2015*, Kissimmee, FL, January 5-9, 2015. doi:10.2514/6.2015-1947.
- [46] Iuliano, E., "Global optimization of benchmark aerodynamic cases using physics-based surrogate models," *Aerospace Science and Technology*, Vol. 67, 2017, pp. 273 286. doi:10.1016/j.ast.2017.04.013.
- [47] Kedward, L. J., Allen, C. B., and Rendall, T. C. S., "Gradient-Limiting Shape Control for Efficient Aerodynamic Optimization," *AIAA Journal*, Vol. 58, No. 9, 2020, pp. 3748–3764. doi:10.2514/1.J058977.

- [48] Kenway, G. K. W., and Martins, J. R. R. A., "Multipoint Aerodynamic Shape Optimization Investigations of the Common Research Model Wing," *53rd AIAA Aerospace Sciences Meeting*, Kissimmee, FL, January 5-9, 2015. doi:10.2514/1.J054154.
- [49] Meheut, M., Destarac, D., Khelil, S. B., Carrier, G., Dumont, A., and Peter, J., "Gradient-Based Single and Multi-points Aerodynamic Optimizations with the elsA Software," *53rd AIAA Aerospace Sciences Meeting*, Kissimmee, FL, January 5-9, 2015. doi:10.2514/6.2015-0263.
- [50] Zingg, D. W., and Elias, S., "Aerodynamic Optimization Under a Range of Operating Conditions," *AIAA Journal*, Vol. 44, No. 11, 2006, pp. 2787–2792. doi:10.2514/1.23658.
- [51] Li, W., Huyse, L., and Padula, S., "Robust airfoil optimization to achieve drag reduction over a range of Mach numbers," *Structural and Multidisciplinary Optimization*, Vol. 24, 2002, pp. 38–50. doi:10.1007/s00158-002-0212-4.
- [52] Poole, D. J., Allen, C. B., and Rendall, T. C. S., "Comparison of Point Design and Range-Based Objectives for Transonic Aerofoil Optimization," *AIAA Journal*, Vol. 56, No. 8, 2018, pp. 3240–3256. doi:10.2514/1.J056627.
- [53] Kraft, D., "A Software Package for Sequential Quadratic Programming," Technical Report DFVLR-FB 88-28, Institut für Dynamik der Flugsysteme, Oberpfaffenhofen, July, 1988.
- [54] Goldberg, D. E., Generic algorithms in search, optimization, and machine learning, Addison-wesley, 1989.
- [55] Clerc, M., and Kennedy, J., "The Particle Swarm-Explosion, Stability and Convergence in a Multidimensional Complex Space," *Evolutionary Computation, IEEE Transactions*, Vol. 6, No. 1, 1995, pp. 58–73. doi:10.1109/4235.985692.
- [56] Kennedy, J., and Eberhart, R., "Particle Swarm Optimization," Neural Networks, 1995. Proceedings, IEEE international conference, Vol. 4, 1995, pp. 1942–1948. doi:10.1109/ICNN.1995.488968.
- [57] Koehler, J. R., and Owen, A. B., Computer experiments, in Ghosh, S. and Rao, C. R. (eds), Handbook of Statistics, Elsevier Science B.V., Amsterdam, 1996.
- [58] Giunta, A. A., "Aircraft multidisciplinary design optimization using design of experiments theory and response surface modeling methods," Ph.D. thesis, Virginia Polytechnic Institute and State University, 1997.
- [59] Santner, T. J., Williams, B., and Notz, W., The Design and Analysis of Computer Experiments, Springer-Verlag, Berlin, 2003.
- [60] Robinson, T. D., Eldred, M. S., Willcon, K. E., and Haimes, R., "Surrogate-Based Optimization Using Multifidelity Models with Variable Parameterization and Corrected Space Mapping," AIAA Journal, Vol. 46, No. 11, 2008, pp. 2316–2326. doi:10.2514/1.36043.
- [61] Koziel, S., "Multi-Fidelity Multi-Grid Design Optimization of Planar Microwave Structures with Sonnet," *International Review of Progress in Applied Computational Electromagnetics*, Tampere, Finland, 2010, pp. 719–724.
- [62] Echeverria, D., and Hemker, P., "Manifold Mapping: A Two-Level Optimization Technique," *Computing and Visualization in Science*, Vol. 11, 2008, pp. 193–206. doi:10.1007/s00791-008-0096-y.

- [63] Echeverria, D., and Hemker, P. W., "Space Mapping and Defect Correction," Comp. Methods in Appl. Math., Vol. 5, No. 2, 2005, pp. 107–136. doi:10.1007/978-3-540-78841-6_8.
- [64] Conn, A. R., Gould, N. I. M., and Toint, P. L., *Trust-Region Methods*, MPS-SIAM Series on Optimization, Philadelphia, PA, 2000.
- [65] Farin, G., Curves and Surfaces for Computer Aided Geometric Design, Academic Press, Boston, MA, 1993.
- [66] Sederberg, T. W., and Parry, S. R., "Free-Form Deformation of Solid Geometric Models," *Proceedings of the 13th annual conference on Computer graphics and interactive techniques*, Dallas, August 18–22, 1986. doi:10.1145/15886.15903.
- [67] Palacios, F., Colonno, M. R., Aranake, A. C., Campos, A., Copeland, S. R., Economon, T. D., Lonkar, A. K., Lukaczyk, T. W., Taylor, T. W. R., and Alonso, J. J., "Stanford University Unstructured (SU2): An Open-Source Integrated Computational Environment for Multi-Physics Simulation and Design," 51st AIAA Aerospace Sciences Meeting and Exhibit, Vol. 2013–0287, Grapevine, Texas, USA, 2013. doi:10.2514/6.2013-287.
- [68] Jameson, A., Schmidt, W., and Turkel, E., "Numerical Solution of the Euler Equations by Finite Volume Methods Using Runge-Kutta Time-Stepping Schemes," *AIAA 14th Fluid and Plasma Dynamic Conference*, Vol. 1981–1259, Palo Alto, CA, June 23-25, 1981. doi:10.2514/6.1981-1259.
- [69] Briggs, W. L., Henson, V. E., and McCormick, S. F., A multigrid tutorial, SIAM, 2000.
- [70] Weller, H. G., Tabor, G., Jasak, H., and Fureby, C., "A Tensorial Approach to Computational Continuum Mechanics using Object-Oriented Techniques," *Computers in Physics*, Vol. 12, No. 6, 1998, pp. 620–631.
- [71] Spalart, P. R., and Allmaras, S. R., "A One Equation Turbulence Model for Aerodynamic Flows," 38th AIAA Aerospace Sciences Meeting and Exhibit, Vol. 92-0439, Reno, NV, January 6-9, 1992. doi:10.2514/6.1992-439.
- [72] Torenbeek, E., Advanced Aircraft Design: Conceptual Design, Technology and Optimization of Subsonic Civil Airplanes, Aerospace Series, Wiley, Chichester, England, 2013.